Contributed paper

OPTO-ELECTRONICS REVIEW 7(1), 29–58 (1999)

Recent advance in semiconductor mid-infrared lasers emitting at 3–12 μm

M. RAZEGHI*

Center for Quantum Devices, Department of Electrical and Computer Engineering
Northwestern University, Evanston, Illinois 60208, USA

In this article, we discuss existing state-of-the-art techniques for the design and fabrication of mid-wave infrared semiconductor lasers (3 μm < λ < 12 μm). Although historically Pb-salt-based lasers had been studied intensively, at the present moment III–V semiconductor lasers are the only viable solution for high power generation of infrared light (P > 300 mW), and thus we focus our study mostly on lasers based on III–V compound semiconductors. Currently, three types of semiconductor lasers are extensively studied in the literature: lasers employing type I interband transition, type II superlattice, and intersubband transitions. Type I interband lasers employing InAsSb/InPAsSb/InAs or InGaAsSb/AlGaAsSb material systems have been most widely studied so far as this type of lasers requires relatively simple and straightforward structures for crystal growth and fabrication. Peak optical output power up to 3 W has been demonstrated for λ > 3.4 μm at 90 K from InAsSb/InAsSbP double heterostructure semiconductor lasers grown by low-pressure metalorganic chemical vapour deposition. Currently, the high-power operation (> 300 mW) for λ > 3 μm from type I interband semiconductor lasers is typically limited to low operating temperatures (below 150 K). Besides Auger recombination which is arguably the major reason for this high temperature sensitivity, the main difficulty in the (Ga)InAsSb-based lasers is the material composition fluctuation associated with large immiscibility gap of the (Ga)InAsSb alloys and the resulting atomic phase separation, which causes spatial inhomogeneity. The effect of the composition fluctuation is formulated in detail. Physical models for emission wavelength, far-field and threshold current are developed and compared with experiment, and magnitude of composition fluctuation is estimated. Room temperature operation for λ > 3.5 μm was achieved from intersubband Quantum Cascade Lasers (QCL) in pulse operation with peak power over 700 mW at 90 K. Yet low quantum efficiency due to fast phonon-related carrier lifetime makes cw operation difficult to perform at the present. We discuss general physical principles, design rules for intersubband QCL are described as well as recent experimental advances. Superlattice mini-band structure, carrier-transport in the presence of electric field will be discussed. Finally we discuss the physical mechanisms and design principles crucial for the device fabrication of bipolar and unipolar type II interband lasers. A more complicated band model should be used compared to intersubband cascade lasers because both wavefunctions of electrons and holes should be considered. Carrier-transport in the presence of electric field will be discussed.

Keywords: mid-infrared lasers, InAsSbP lasers, quantum cascade lasers, device performance.

1. Introduction

Mid-infrared laser diodes (λ = 3 to 12 μm) are the integral part in a wide range of applications from chemical spectroscopy, to free-space and optical fiber communications [1,2]. These lasers provide very sensitive detection of gases because many atmospheric molecules have strong absorption lines in this wavelength band. The lasers provide measurement capabilities far beyond that of conventional instruments. Midwave- and longwave-infrared regions are important in many military and civilian applications because of the atmospheric transmission windows in these wavelengths. These atmospheric windows make ultralow loss free-space communication possible with much higher bandwidth and higher selectivity of receivers compared to the conventional microwave communication. It also has been suggested that

* e-mail: razeghi@ece.nwu.edu

heavy-metal fluoride fibers may have a few orders of magnitude lower optical loss at $\lambda = 2 \sim 3$ μm [3] than the widely used silica fibers, suggesting the use of mid-infrared lasers in future optical fiber communication.

The first midwave-infrared laser operation was demonstrated from Pb-based IV–VI semiconductor lasers [4,5] and the room temperature operation was achieved from $PbSe/Pb_{1-x}Sr_xSe$ double heterostructure (DH) lasers at emission wavelength 4 to 5 μm in 1988 [6,7]. However, the Pb-salt lasers developed have been shown to be problematic in achieving high power, high efficiency, and/or high reliability, and output power is typically lower than 1 mW. These problems presumably originate from weak bonding characteristic of IV-VI (rock-salt structure) semiconductors, which results in poor mechanical strength and thermal stability.

To date, a number of other material systems and laser structures have been proposed as alternatives to Pb-based IV–VI materials. A number of III–V semiconductor alloys, benefiting from stronger covalent bonding and advanced growth and device processing technology, have been investigated. For wavelengths shorter than 3 μm, great improvements in laser performance have been achieved recently. Threshold current as low as 40 A/cm^2 was achieved at room temperature for $\lambda = 2$ μm MBE-grown GaInAsSb/AlGaAsSb QW lasers [8]. In general, however, performance degrades rapidly with the increase in emission wavelength as the GaInAsSb composition corresponding to longer wavelength is thermally unstable, and tends to undergo phase-separation instead of forming uniform randomly mixed alloys. To date no room temperature operation has been reported for $\lambda > 3$ μm.

For high power mid-infrared lasers with emission wavelengths of 3 to 5 μm, the III–V ternary $InAs_{1-x}Sb_x$ is a superior material compared to InGaAsSb quaternary, due to fewer immiscibility problems in the former. Extensive research has been done for the fabrication of high power, room temperature operation of the lasers based on InAsSb [9–11]. Output power up to 3 W has been demonstrated recently from InAsSb/InAsSbP heterostructure lasers at 90 K [11–13]. However, high temperature-sensitivity of the laser characteristics is the major problem for III-V compound-based lasers as in other lasers based on IV–VI or II–VI compounds. So far these high performance infrared semiconductor lasers for $\lambda > 3$ μm (with output power > 300 mW) are typically limited to low operating temperatures (below 150 K). Extremely high temperature sensitivity (T_o as low as 20 K) is often observed, which results in very high J_{th} at high temperatures (e.g., $J_{th} > 10$ kA/cm^2 above 200 K). A number of physical mechanisms have been proposed to explain the high temperature sensitivity of this kind of lasers. Auger recombination, leakage current, or intervalence band absorption are among the most widely suggested explanations. However, so far no direct experimental analysis has yet been performed to directly confirm the significance of these mechanisms to the high temperature sensitivity of these lasers.

These conventional lasers are based on type interband transition, and the emission wavelengths are essentially determined by the energy gap of the semiconductors used, and therefore have rather limited capability for tuning of emission wavelength. The fabrication of the lasers is relatively straightforward provided the materials (often exotic) can be grown with high reproducibility. Beside this type of lasers, novel kinds of laser structures have recently emerged. One type of them uses type II superlattices. Here, type II superlattice means a superlattice consisting of two or more alternating thin layers with staggered energy gaps, that is, both conduction and valence band energy levels of one material are lower than those of other alternating materials. The most prominent example of this structure are the $Ga_xIn_{1-x}Sb/InAs$ superlattices [14,15], where $Ga_xIn_{1-x}Sb$ has both higher conduction and valence bands compared to InAs. In this case, the primary radiative recombination occurs between electrons in InAs and holes in GaSb sides, and the emission photon's energy is lower than either of energy gaps of InAs and GaInSb, and can be controlled by interface layers between them, doping level (which controls the electric field between the two regions) and composition of active alloys layers. Another class of lasers utilizes intersubband transition [16]. In this type of lasers, which is named quantum cascade lasers due to the use of multi-stage cascaded active regions, the emission wavelength is determined by the intersubband transition in quantum wells, and thus gives much higher freedom in selecting emission wavelengths, particularly for wavelengths longer than 5 μm. This type of lasers showed near-room temperature laser operation in pulse mode for $\lambda = 3$ to 13 μm. However, the complicated structures (requiring many stages of growth of superlattices) and the resulting low yield may be the major challenges in these lasers. Furthermore, the power conversion efficiency is considerably lower than their conventional (i.e., based on direct interband

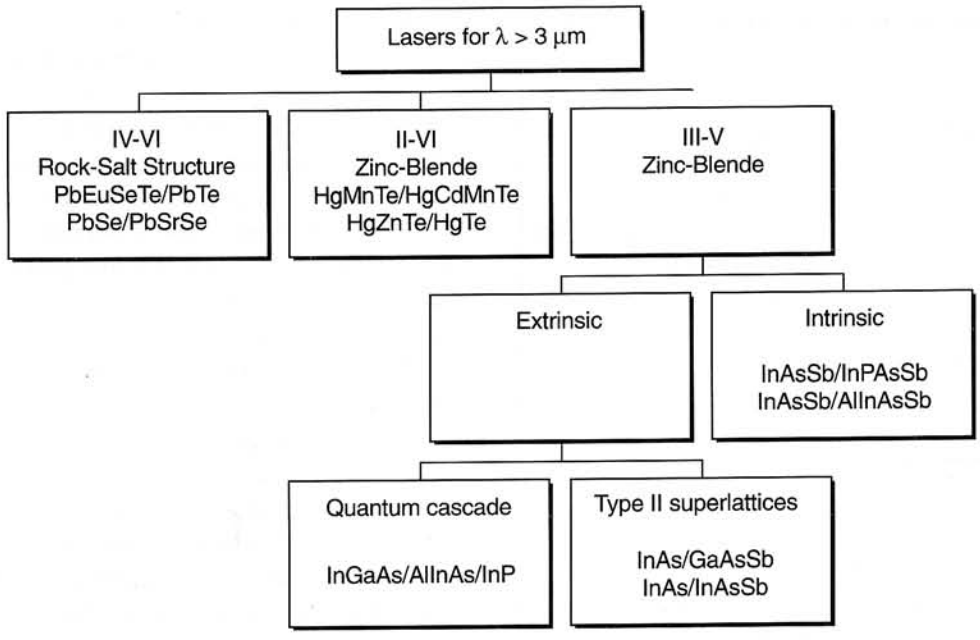

Fig. 1. Classification of infrared lasers. Type II lasers and quantum cascaded lasers are classified as "extrinsic lasers" in this work to distinguish from "intrinsic lasers" whose emission wavelengths are determined essentially by energy gap.

transition) counterparts. Figure 1 schematically shows the classification of infrared semiconductor lasers. Advantages and disadvantages of each material system are summarized in Table 1. Lasers based on type I interband, type II interband, and type I inter-subband radiative transitions are compared in Fig. 2, showing the maximum output power for each type of lasers at room temperature, Fig. 2(a) and 77 K, Fig. 2(b). These figures clearly indicate that the lasers have somehow complementary characteristics: that is, lasers based on type I interband transition (like InAsSb/InAs or InAsSb/InGaAsSb lasers) have generally high maximum CW output power, indicating high output efficiency and thus lower device heating. For lasers based on type II and intersubband transitions CW operation is limited to low temperatures, presumably due to low power conversion efficiency (typically less than a few percent).

Table 1. Comparison of material systems for mid-infrared lasers.

	Advantages	Disadvantages
IV–VI	• Availability of low-gap materials (λ ~ 3-30 μm) • Large energy-gap cladding layers lattice-matched to the low-gap materials	• Poor mechanical and thermal properties limit maximum power to a few mW at low temperatures
II–VI	• Availability of low-gap materials • HgTe and CdTe have very close lattice constants	• Poor mechanical and thermal properties prevent high-temperature operation • Instability due to high mobility of Hg atoms
III–V Intrinsic	• Availability of mature growth and processing technologies • Strong covalent bonding allows good mechanical and thermal properties	• No proper lattice-matching confinement layers for λ > 3 μm
III–V based Type II	• Low Auger recombination rate • Wavelength control free from lattice-match constraints	• Large number of layers • Sensitive to the interfaces
III–V based Quantum cascade	• Use of mature InP growth technologies • Wavelength control free from lattice-match constraints	• Complicated design and growth • (> 20 stages of superlattice have to be precisely controlled)

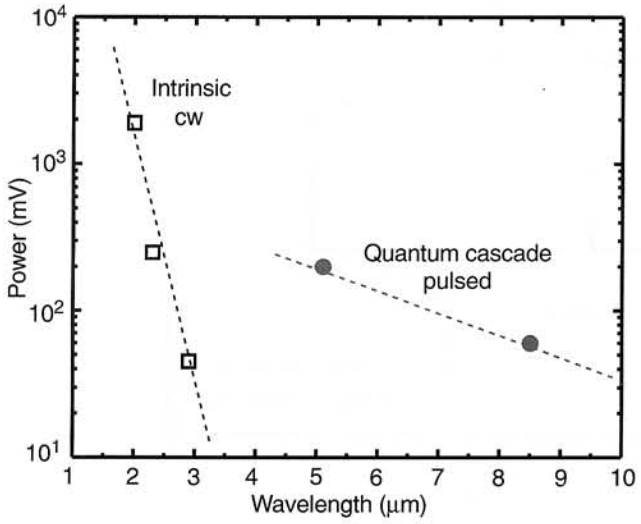

Fig. 2(a). Maximum output power at room temperature (cw or pulse) vs emission wavelength. Here open squares (❑) indicate the maximum cw output power of InGaAsSb/AlGaAsSb type I interband (intrinsic) QW lasers reported in the literature. The closed circles (●)represent the maximum pulse output power of InGaAs/InAlAs QCL. Note that CW operation has not been reported for QCL at room temperature. Dotted lines are guide-to-eyes.

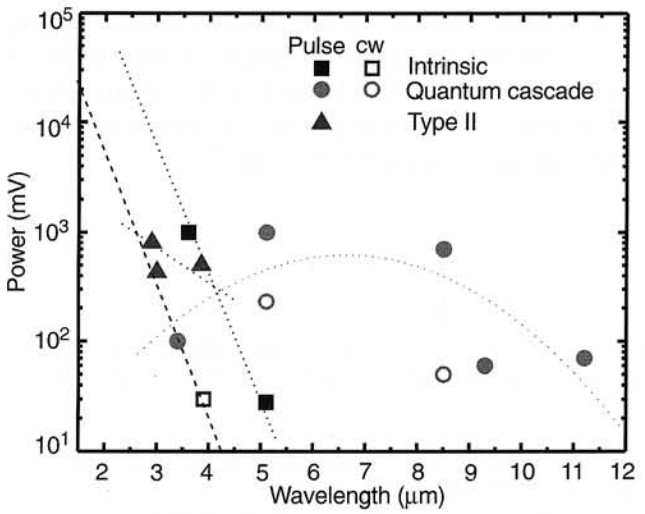

Fig. 2(b). Maximum output power at 77 K (cw or pulse) vs emission wavelength. Here open square (❑) and closed squares (■) indicate the maximum cw and pulse output powers of InGaAsSb/AlGaAsSb, InAsSb/InPAsSb, or InSb/InAlSb type I interband (intrinsic) lasers reported in the literature, respectively. The open circles (○) and closed circles (●) represent the maximum cw and pulse output power of InGaAs/InAlAs Qunatum Cascade Lasers (QCL), respectively. The closed triangles (▲) represent pulse output power of type II InAs/GaInSb superllatice laser diodes (electrically pumped). No cw operation has been reported for type II laser diodes. The dotted lines are guide-to-eyes.

The purpose of this article is to provide detailed exposition of the existing semiconductor technologies for the mid-infrared lasers. Lasers based on type I interband, type II interband, and inter-subband transitions are compared, and their respective advantages and disadvantages are discussed. In section 2, we will focus on high-power type I interband semiconductor lasers (> 300 mW) for $\lambda > 3$ μm, particularly InAsSb/InPAsSb-based lasers. One of the major difficulties in the Sb-containing alloys-based lasers is the material composition fluctuation associated with large immiscibility gap of the (Ga)InAsSb alloys and the resulting atomic phase separation, which causes spatial inhomogeneity. The effect of the composition fluctuation is formulated in detail. Physical models for emission wavelength, far-field and threshold current are developed and compared with experiment, and magnitude of composition fluctuation is estimated. Recent progress in device performance of the type I interband lasers are also discussed. In section 3, general physical principles, design rules and recent experimental advances for intersubband Quantum Cascade Lasers (QCL) are described. Superlattice mini-band structure and carrier-transport in the presence of electric field will be discussed. In section 4, we discuss the physical mechanisms and design principles crucial for the device fabrication of bipolar and unipolar type II interband lasers. A more complicated band model should be used compared to intersubband cascade lasers because both wavefunctions of electrons and holes should be considered. Carrier-transport in the presence of electric field will be discussed. Brief summary is given in section 5.

2. Type I interband-transition InAsSbP lasers

2.1. Historical background

Shortly after the observation of stimulated emission from GaAs diode [17,18,19], laser operation was observed from Zn-diffused [20] and LPE-grown [21] InAs diode at T = 4 ~ 77 K. At the same period, optically pumped pulsed laser emission at 3 μm from InSb was observed at liquid helium temperature [22]. In 1966 the first InAsSb pn homojunction laser operation was achieved at $\lambda > 3$ μm below liquid nitrogen temperature [23].

Initially Al-based higher band gap materials such as AlGaSb, AlInSb have been considered for the cladding layers. The InAs-based InAsSb/InAlAsSb MQW laser has exhibited maximum operation tem-

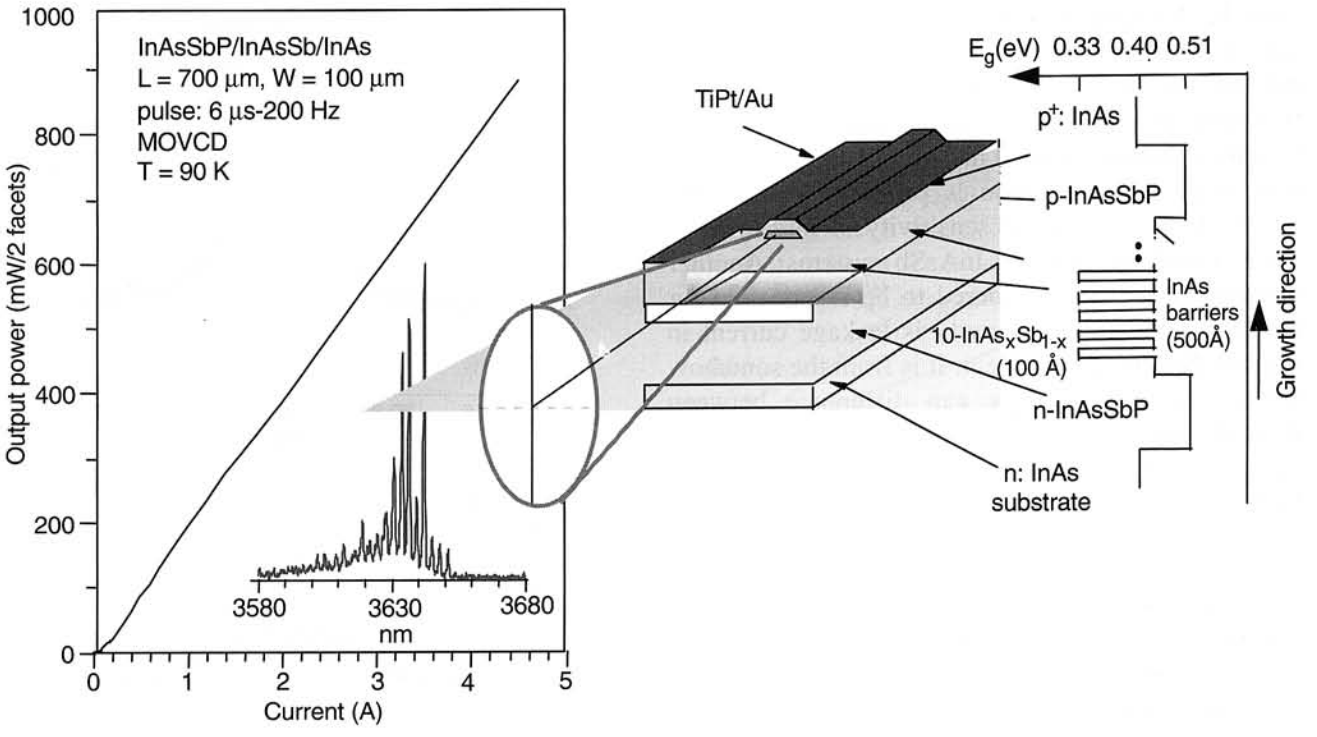

Fig. 3. Optical power vs injection current curve (P–I curve) from an InAsSb/InPAsSb MQW laser measured at 90 K; (Inset) Laser emission spectrum at 90 K; (Right) Schematic diagram and energy gap profiles of the laser diodes.

perature of 225 K in pulse mode at an emission wavelength of 3.5 μm [9,24]. However, it was soon realized that they have problems related to unfavorable type II band alignment with InAsSb which prevent the efficient carrier confinement, and/or small difference in refractive indices in the heterostructure. Unlike Al-based higher band-gap materials, the Al-free quaternary InPAsSb material system provides a very favorable condition for the carrier and optical confinement due to its type I band alignment and lower refractive index of the higher band gap materials, and excellent dopant incorporation [11,13,25,26], thereby providing efficient injection and carriers confinement. However, like other Sb-based alloys, it is well known that the InP(As)Sb is thermodynamically unstable at typical growth temperatures against phase separation [27,28]. The problem of thermodynamic instability, however, can be overcome by growing these materials in non-equilibrium growth modes, using such as MBE and MOCVD, and high material quality of InAsSb and InPAsSb and DH and MQW lasers based on these materials have been achieved recently by Lane et al. using MOCVD [11]. These high quality lasers have generated high output power up to 1 W at 90 K, Fig. 3. This output power is about 1000 times higher output power compared to the optical output power of typical Pb-salt (IV–VI) compounds based lasers (~ 1 mW). This high performance results from the advantage of III–V compound technologies related to the strong mechanical hardness and high thermal conductivity resulting from strong covalence bonding nature, and high quality growth of crystal. This result strongly indicates that InAsSb/InPAsSb mid-infrared lasers are an excellent candidate for the high power infrared light sources. As discussed in Introduction, the primary problem in the mid-infrared lasers is the extremely high sensitivity of laser characteristics on temperature. For example, threshold current density increases by 2 or 3 orders of magnitude with an increase in temperature from 78 K to 220 K. Because of this prohibitively high J_{th}, to date, room temperature operation of mid-infrared based on III–V compounds based on interband transition has not been achieved yet in spite of their promising high power operation capability at low temperature.

Auger recombination rate is strongly dependent on temperature and energy gap. It is because both energy and momentum conservation are readily satisfied within the thermal uncertainty as energy scale involved in the transition (order of energy gap) is comparable to thermal energy. Previously developed theories [29,30] had shown that for InAs or GaSb,

those having spin-split energy comparable to energy gap (E_g) can have very high Auger recombination due to the efficient energy transfer from electron-hole recombination to excitation of heavy holes to spin-split band. Thus it has been widely suggested that Auger recombination is primarily responsible for the high temperature sensitivity of mid-infrared lasers based on InAs or InAsSb systems. Another mechanism that is considered to be responsible for the high temperate sensitivity is leakage current in the InAsSb/InPAsSb system. It is from the somehow limited range of energy gap difference between InAsSb active layer and InPAsSb cladding layer ($\Delta E_g \sim 120$ meV). Other mechanism that might lead to the high temperature sensitivity is the increase in optical loss of the lasers with temperature. Considering the fact that spin-slitting energy of InAsSb is comparable to its band gap energy E_g, and thus the intervalence band absorption may be significant in this material with a strong temperature dependence [31], the possibility that the high J_{th} may result from the high radiative recombination current cannot be entirely excluded.

2.2. Characterisation and devices performance of InAsSbP lasers

In this subsection, we will be primarily focused on lasers based on InAsSbP/InAsSb material systems as these are one of the promising material systems for high power lasers as described above. The typical x-ray diffraction patterns and photoluminescence of InAsSbP/ InAsSb heterostructures are shown in Figs. 4 and 5, respectively [11]. In Fig. 4(b), we compare experimental x-ray diffraction pattern (middle) of MQW lasers with those obtained by simulation employing bi-layer model (top) and four layer model including InSb interface layers (bottom). This comparison shows that interface layers are formed during growth of thin InAsSb quantum wells. Figure 5(b), which shows photoluminescence of $InAs_xSb_{1-x}$/InAs(SbP) MQW structure with different $InAs_xSb_{1-x}$ compositions that cover the entire 3 to 5 μm range, demonstrates that high quality multilayer structures have been grown and that the structures can be engineered for desired emission wavelengths covering the entire mid-infrared region. Broad-area laser diodes are typically fabricated using lift-off process, in which the cap layer is etched away between the metal contact stripes composed of Ti/Pt/Au. Thermal treatment of the ohmic contacts usually is performed at elevated

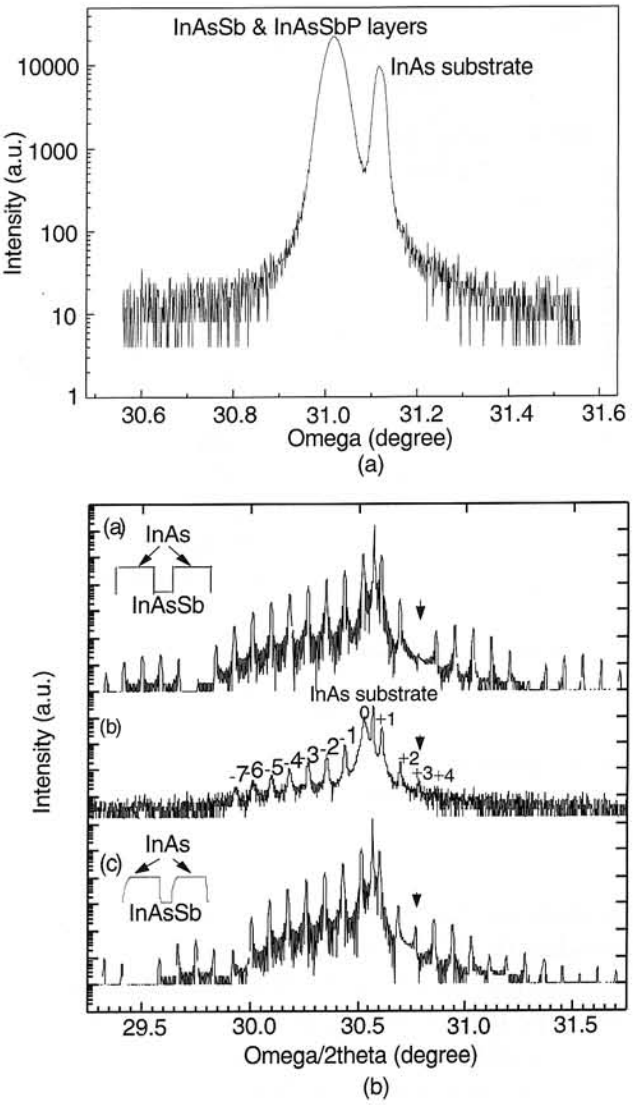

Fig. 4. X-ray diffraction pattern of InAsSb/InAsSbP (a) DH and (b) MQW lasers [(top) simulated pattern with bi-layer model, (middle) measured pattern and (bottom) simulated with four layer model].

temperatures to obtain a low resistance of 0.2 Ω at 79 K [11].

Maximum output power increases almost linearly with the increase of the total aperture (~ number of stripes), as shown in Fig. 6. A laser bar with total aperture of 200 μm (2 × 100 μm) generated optical power of up to 1.85 W, while a laser bar with 3 stripes up to 3 W. For a 3-stripe laser bar (total aperture width of 300 μm), the maximum output power was limited by our current generator (< 30 A), Fig. 6, [32]. The linear increase of the maximum output power with total aperture also indicates that current is injected uniformly, with a maximum of 10 A per 100-μm wide stripe. Since the series resistance R_s of a 100-μm aperture laser diode based on this material is

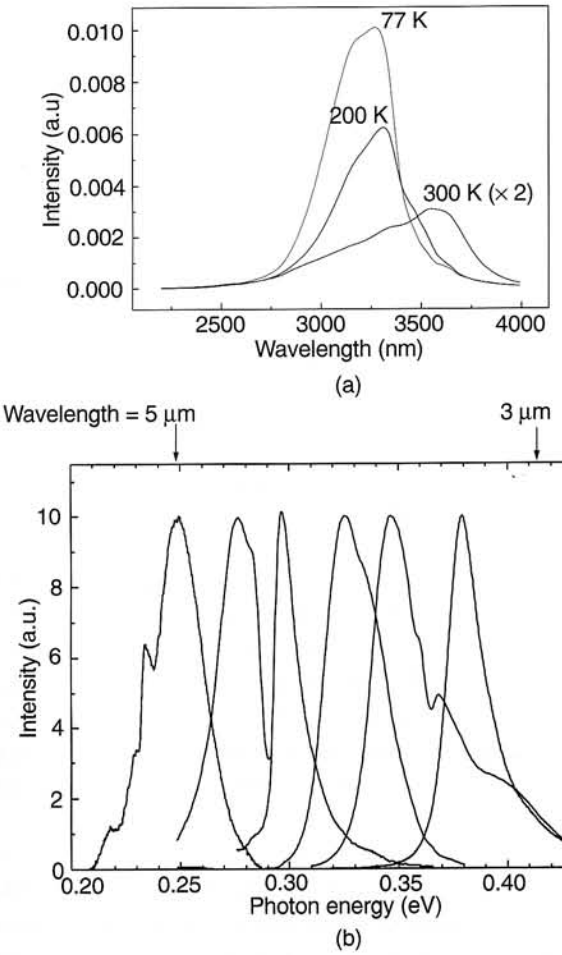

Fig. 5. Photoluminescence spectrum (a) of an InAsSb/InAs DH structure as a function of temperature and (b) $InAs_xSb_{1-x}$/InAs(SbP) MQW structure with different $InAs_xSb_{1-x}$ compositions that cover the entire 3 to 5 μm range.

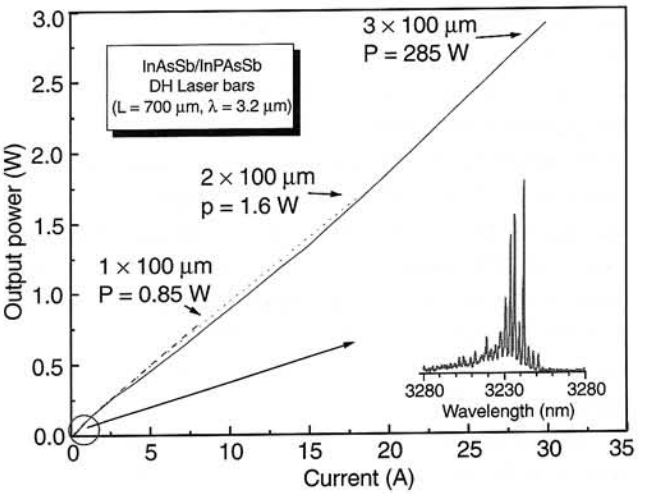

Fig. 6. PI curves of the laser bars with stripe width of 1×100, 2×100, and 3×100 μm.

about 0.23 Ω [33], the Joule heating at each stripe at the maximum current is $R_sI^2 \approx 0.23\ \Omega \times (10\ A)^2 \approx 23$ W, which is much higher than the optical power (~ 1 W). This estimation indicates that the Joule heating may be the most important factor responsible for the device failure at high power operation. The reduction of series resistance or the design of a novel structure enabling efficient heat dissipation is, therefore, a critical technological challenge for the laser operation with higher output power per aperture.

The major potential problem in using large-aperture light sources is the degradation of beam quality due to induced and/or residual material non-uniformity. As a result, a laser bar may not emit light with a narrow spectral width or narrow directional angle

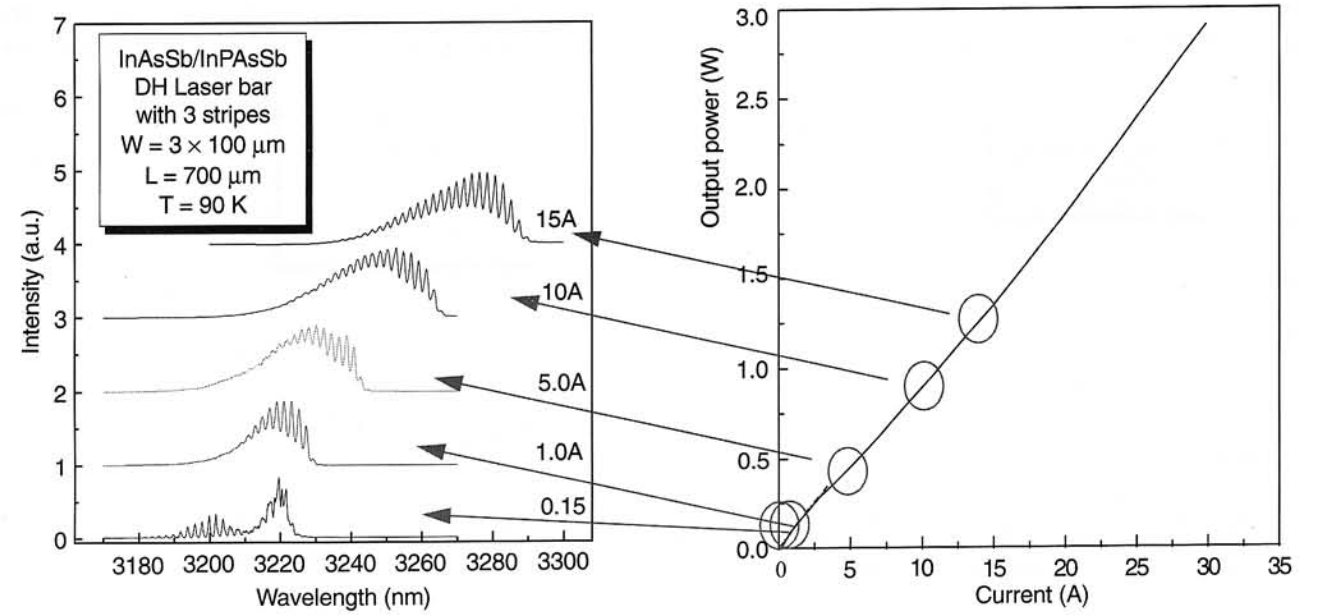

Fig. 7. Spectra of a 3–stripe laser bar for various injection currents.

(far-field beam divergence), and therefore the high--power obtained from the device would be utilized only partially in some applications. Figure 7 shows the emission spectrum of a laser bar with three stripes (total aperture of 300 μm) measured within a current range of 0.15 A to 15 A at 90 K. Despite the large total area of the device (900 μm × 700 μm), the spectrum remains quite regular at high currents, resembling that of a single-stripe laser. This result indicates that the LP-MOCVD-grown wafers have highly uniform composition across large areas [34], making them suitable for large-scale industrial manufacturing.

The peak of emission spectrum shifts to longer waves with an increase in current. This indicates a significant heating caused by the high current injection, consistent with the estimation of Joule heating discussed above. The shift of wavelength, $\Delta\lambda$, as much as 70 nm has been observed with the increase of current, ΔI, by 15 A. Previously, it was shown that the shift of energy gap with an increase in temperature, $\Delta\lambda/\Delta T$, is about 1.25 nm/K [35]. Thus, $\Delta\lambda$ of 70 nm at I = 15 A current injection corresponds to 55 K of the increase in junction temperature. It is likely that some regions of different resistance (due to defects, etc.) can have even higher temperature, initiating the device failure with a positive feedback effect similar to the mirror damage mechanism (e.g., increasing the optical absorption or non-radiative recombination, which further increases local temperature) [36].

The far-fields of a laser bar in the direction perpendicular to the junction for a wide range of injection currents are shown in Fig. 8. Remarkably, far-fields in the direction perpendicular to the junction as narrow as 12° (FWHM) were measured (Fig. 8). These measurements were repeated with a

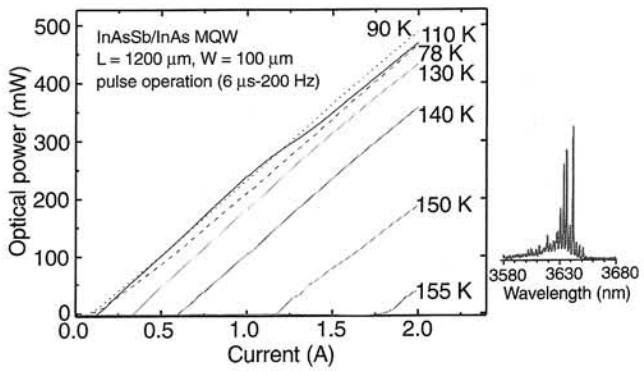

Fig. 9. Temperature dependence of PI characteristics of InAsSb/InPAsSb MQW lasers (λ = 3.6 μm); (Right) Emission spectrum of an InAsSb/InPAsSb MQW laser.

number of lasers processed from the same wafer, and similar values of far-field beam divergence (10–15°) were obtained. We have estimated that the measured far-fields' FWHM could be up to 5° less than the true perpendicular far-field FWHM. This difference has been estimated taking into account the following sources of error: plane of scanning not exactly along the direction of maximum width, and interference, angle-dependent reflection, and feedback effects introduced by a cryostat window. These narrow far-fields are in a considerable discrepancy with the prediction based on classical theoretical models [37]. According to the slab waveguide model [37], this far-field of 12° (FWHM) corresponds to the refractive index difference, Δn, between the active layer (InAsSb) and cladding layers (InPAsSb) of less than 0.03, which is too small compared to values obtained elsewhere (e.g., from interpolation based on refractive indices of the binary constituents [35]). At present, the physical ori-

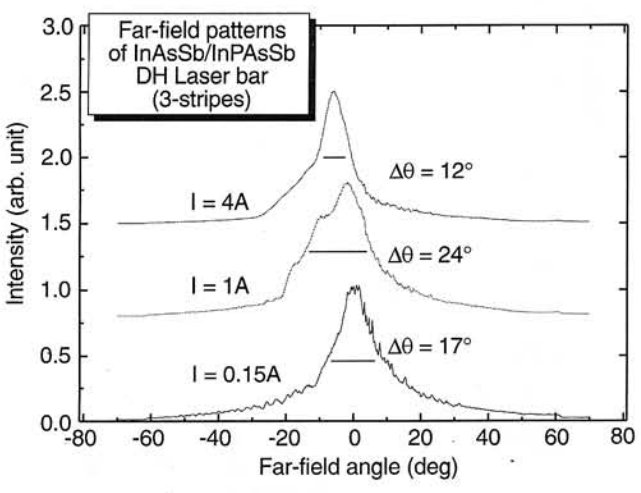

Fig. 8. Far-fields of a 3–stripe laser bar for various injection currents.

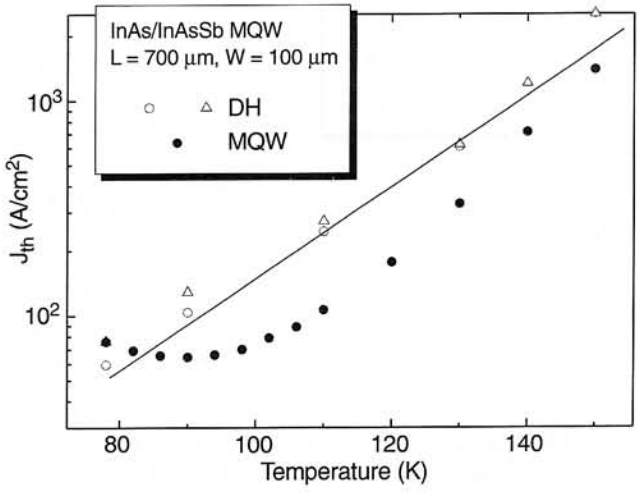

Fig. 10. Temperature dependence of J_{th} of MQW lasers and DH lasers for cavity lengths of 700 μm.

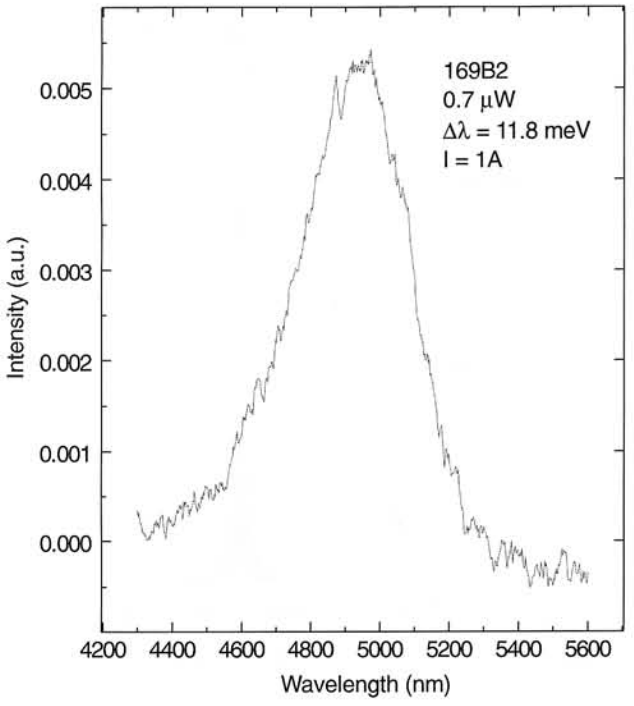

Fig. 11. Electroluminescence spectrum of an InAsSb/InAs MQW structure with center wavelength λ = 5 μm.

gin of such narrow far-field patterns in the perpendicular direction has not been explained, but some of our measurements suggest that doping may have played a significant role in changing the refractive index much more than in other materials. Figure 9 shows P-I curves of the InAsSb/InPAsSb MQW lasers with emission wavelength of 3.6 μm measured between T = 78 K and 155 K. The differential efficiency remains above 70% up to 155 K. Threshold current density J_{th}, however, has very strong temperature dependence as shown in Fig. 10. Typical T_o is only about 20-40 K.

For wavelengths longer than 4 μm, we have extended the emission wavelength by increasing Sb composition in the quantum well. The resultant increase in compressive strain of the quantum wells makes the growth of high quality InAsSb active region difficult. Nevertheless, high luminescence-efficiency light sources were grown. Figure 11 shows the electroluminescence spectrum of primary MQW InAsSb/InAs/InPAsSb structures with emission wavelengths of 5 μm, with maximum power of around 1 μW. The bright and narrow-width electroluminescence from the primary MQW structures presents the promising potentials of the MOCVD-grown InAsSb/InPAsSb heterostructures for the mid-infrared lasers for deep mid-infrared ranges.

2.3. Effects of composition fluctuation on laser characteristics

One of the difficulty in the (Ga)InAsSb-based lasers is the material composition fluctuation associated with large immiscibility gap of the (Ga)InAsSb alloys and the resulting atomic phase separation, which causes spatial inhomogeneity. Recent TEM measurements [38] have shown that MOCVD-grown $InAs_{1-x}Sb_x$ alloy exhibits a partial degree of phase separation that leads to composition inhomogeneity with a characteristic length about 100 nm in the growth plane, for a wide range of growth conditions. It was also shown [12] that dependence of threshold current density on cavity length observed in the InAsSb/InPAsSb DH lasers could not be explained without the effect of compositional inhomogeneity. Thus, one of the important factors in modeling and design of lasers with substantial alloy immiscibility gap as in InAsSb and InPAsSb is the proper consideration of the alloy composition fluctuation. In this subsection we will illustrate how to incorporate these effects. Physical models for emission wavelength, far-field and threshold current are developed and compared with experiment, and magnitude of composition fluctuation is estimated.

2.3.1. Modelling of the effect of δn on emission spectrum

Fabry-Perot modes observed in emission spectrum of lasers result from resonance of longitudinal directional laser beam in cavity. The spacings between Fabry-Perot modes are usually equal, and determined by cavity length L and refractive index N of the cavity (= $c\pi/NL$, where c is the speed of light in vacuum). However, as will be shown below, when the cavity has significant refractive index fluctuation, each longitudinal mode "sees" different effective cavity length, and therefore, the resonance frequencies are shifted by different amount. As a result, the mode-spacings are no longer equal, and show significant random emission spectrum structure. The left column of Figure 12(a) shows the experimental emission spectrum of InAsSb/InPAsSb DH lasers with different cavity length fabricated from a single wafer. The right column shows the dependence of emission spectrum on injection current for the laser with cavity length of 700 μm. The most striking feature of this measurement is that with increase in current, the emission spectrum becomes broadened and Fabry-Perot spacing almost cannot be resolved. The laser

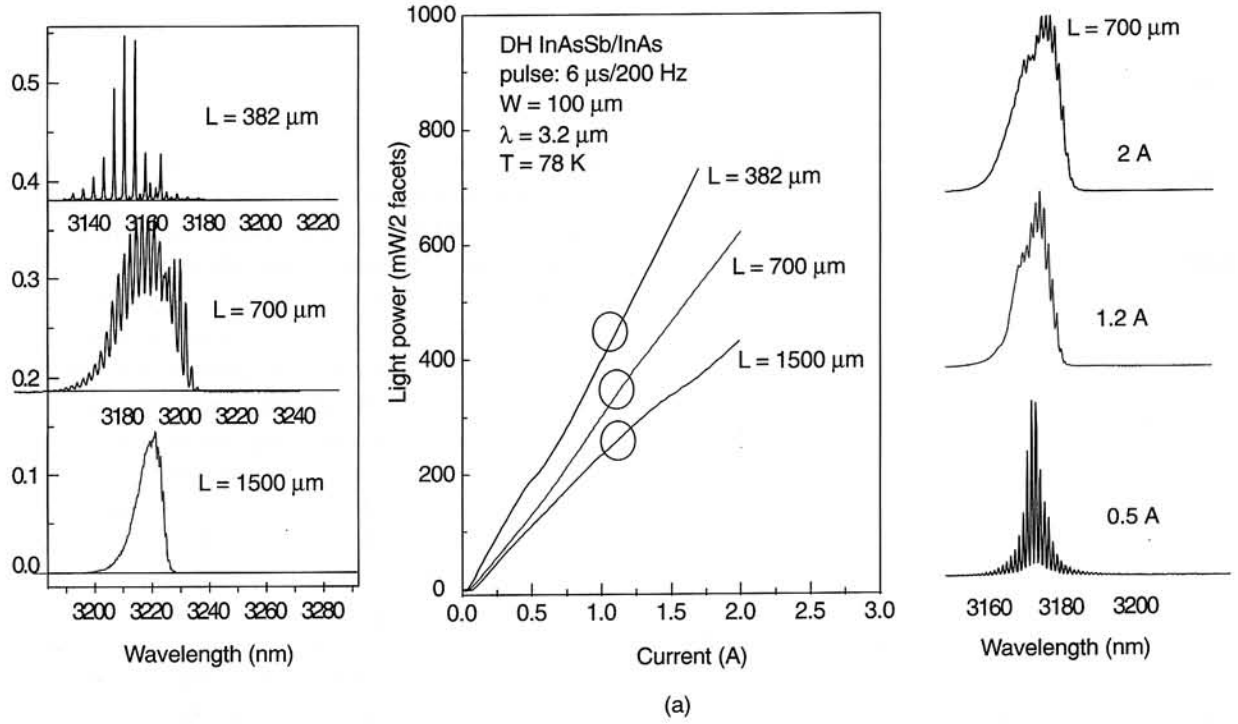

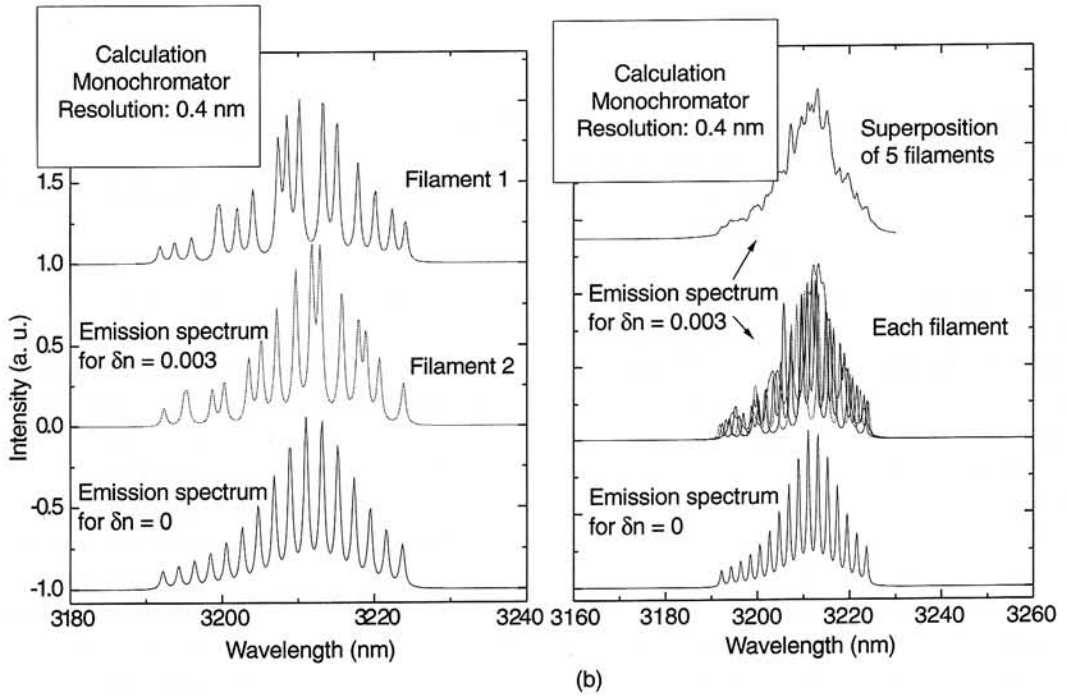

Fig. 12. Emission spectrum of InAsSb/InPAsSb DH lasers (λ = 3.2 μm); (a) experimental emission spectrum as a function of cavity length (Left) and current injection (Right); (b) calculation showing the spectrum of filaments within a broad-area laser with $\langle \delta n \rangle = 0.003$ (Left); Resulting emission spectrum of a laser consisting of 5 filaments with $\langle \delta n \rangle = 0.003$ (Right); Emission specta for lasers with homogeneous composition are marked $\delta n = 0$.

was injected with a pulse of 5 μs width; and the measurement was performed with a boxcar with a much narrower time window (< 1 μs), and thus we exclude the possibility that the broadening comes from the temporal average of spectrum due to the change of temperature. In this subsection, we will present a simple model calculation explaining that this results from the refractive index fluctuation, and its temperature dependence. Firstly, it will be described how the effect of refractive index fluctuation affects the longitu-

dinal resonance frequencies. As this feature may be revealed in many lasers with significant refractive index fluctuation, this modeling can be applied to other types of lasers without modification. The problem of longitudinal mode resonance frequency in cavity with refractive index fluctuation can be modeled by solving Maxwell's equation with media possessing refractive index fluctuation $n_o + \delta n(\mathbf{r})$

$$\nabla^2 \boldsymbol{E} + [n_0 + \delta n(r)]^2 \frac{\omega^2}{c^2} \boldsymbol{E} = 0 \tag{1}$$

where n_o, $\mathbf{E}$, ω, c are the refractive index, electric field, optical frequency, and the speed of light, respectively. $\delta n(r)$ is a random distribution with a given $\langle \delta n \rangle$ and correlation length ($\langle \bullet \rangle$ denotes standard deviation). Now, by expanding the electric field E using "unperturbed optical modes" $\varphi_n(z)$, i.e. $E = \sum_n A_n \varphi_n(z)$ to Eq. (1), where

$\varphi_n(z) = \sqrt{2/l} \sin k_n z [k_n \equiv (\pi/L)n]$, yields

$$\sum_n [(-k_n^2 + n_o^2 \omega_n^2)\varphi_n(z) A_n + \Delta n(z)^2 \omega_n^2 \varphi_n(z) A_n] = 0 \tag{2}$$

where $\Delta n(z)^2 \equiv 2 n_o \delta n(z)$. By multiplying $\varphi_m^*(z)$ and integrating over the cavity length, and using the orthonormality relation $\int_0^L \varphi_m^*(z)\varphi_n(z) = \delta_{nm}$, we obtain

$$\left[\frac{(n_o^2 \omega_m^2 - k_m^2)}{n_o^2 \omega_m^2} A_m + \sum_n K_{mn} A_n \right] = 0 \tag{3}$$

where

$$K_{mn} \equiv \int_0^L \varphi_m^*(z)\varphi_n(z) \frac{\Delta n(z)^2}{n_o^2} \varphi_n(z) \tag{4}$$

In other form, it can be considered to be an eigenvalue problem:

$$\sum_n K_{mn} A_n = \lambda_m A_m \tag{5}$$

where

$$\lambda_m = \frac{(k_m^2 - n_o^2 \omega_m^2)}{n_o^2 \omega_m^2}. \tag{6}$$

Thus, by solving the eigenvalues λ_m of Eq. (5), we can calculate ω_m, the eigenfrequency of m^{th} mode in the presence of refractive index fluctuation $\delta n(z)$ from Eq. (6).

In order to have tractable numerical solution, we have approximated n(z) as follows:

$$\delta_n(z) = \delta n_i \quad \text{for} \quad l_{i-1} \le z < l_i \tag{7}$$

where i is the integer such that $1 \le i \le \alpha$ and l_i is random variable such that $0 = l_0 < l_1 < l_i < l_\alpha = L$, and δn_i is the constant such that $\sqrt{\sum_i \delta n_i^2 / \alpha} \equiv \delta N$ (constant) with average zero. Then

$$K_{mn} = \frac{2\delta n_i}{n_o} \frac{2}{L} \mathrm{Re} \sum_{i=1}^{\alpha} \int_{l_i - 1}^{l_i} dz \exp(i \Delta k_{mn} z) = \\ = \frac{2\delta n_i}{n_o} \frac{2}{i \Delta k_{mn} L} [\exp(i \Delta k_{mn} l_i) - \exp(i \Delta k_{mn} l_{i-1})] \tag{8}$$

where $\Delta k_{mn} = k_m - k_n$. The remaining numerical calculation procedure is as follows: Firstly, the random variable δn_i and l_i series are generated according to Gaussian distribution with standard deviation of $\delta N = 0.003$ and $\langle l \rangle = 100$ nm (also average), respectively. Then K_{mn} was calculated from Eq. (7), and then eigenvalues λ_m were obtained from the eigensystem Eq. (5). The eigenfrequencies ω_m were finally obtained from Eq. (6). These ω_m correspond to the modified Fabry-Perot mode of the laser with δn. With the obtained ω_m, emission spectrum was obtained from a Green's function model developed previously [30]. The calculated ω_m was used to obtain the emission spectrum with the broadening of each Fabry- -Perot mode being assumed to follow Lorenz function whose shape is essentially determined by monochromator resolution, about 0.4 nm in our measurement. We assumed that the whole envelop of the emission spectrum is also given by Lorenztian function with half width of about 20 nm, which is about the values observed in the experiment. The calculation results are shown in Fig. 12(b). Unlike emission spectrum for homogeneous cavity ($\delta n = 0$), that for cavity with a finite δn (= 0.03 in this calculation) shows that spacing between each Fabry-Perot mode (resonance mode in the cavity) is not regular, and is strongly dependent on the actual $\delta n(z)$ distribution [see two left upper spectra of Fig. 12(b)]. Since a broad-area laser consists of several incoherent laser emission sources due to filamentation, the emission spectrum will be superposition of those from each region that has different $\delta n(z)$ distribution. Right upper spectrum of Fig. 12(b) shows the superposition of spectrum from each region, which results in a very broad spectrum and no resonance-modes could be resolved, as consistent with experimental results. As will be shown below, refractive index fluctuation increases with temperature and current due to high local-temperature

sensitivity of refractive index. The present study indicates that refractive index fluctuation increases with current, significantly affecting emission spectrum, and thus laser structure should be carefully designed and fabricated for high temperature operation of lasers.

2.3.2. Modeling of effect of δn on far–field

Refractive index fluctuation can have significant effect on the far-field pattern of the InAsSb/InPAsSb lasers. Figure 13(a) shows the measured far-fields of the DH lasers for various injection currents and operating temperatures reported by Yi et al. [39]. The far-fields are found to broaden rapidly as the temperature (and current) increase above 120 K, contrary to the conventional theory where far-field is almost independent of temperature. With the broadening of far-fields, several satellite peaks appeared. The overlaying of these far-fields [bottom of Fig. 13(a)] shows that the far-field has widened by about 50% at 130 K compared to that at 78 K. These measurements were repeated for 3 additional DH lasers (λ = 3.2 μm) with a similar structure. The dependence of far-fields on temperature and current similar to Fig. 13(a) was exhibited in all the DH lasers. The InAsSb/InPAsSb/InAs DH lasers were examined with SEM, and no noticeable roughness was found in the mirror facets. Since the measurements were performed with diodes located in a cryostat, it may be suspected that the far-fields were affected by interference of the emitted light with the cryostat window (sapphire) or feedback from the reflected light. The interference and feedback effects were examined by various positioning of the laser with respect to the cryostat window. Except for a narrow angle range (close to normal incidence), the far-fields were not affected by the change of the incident angle. Finally, our measurement system was tested with other types of lasers. Clean Gaussian-like far-fields were obtained from near-infrared lasers (InGaAsP/GaAs, λ = 0.808 μm) using the same measurement set-up [40]. The above facts consistently indicate that the distorted far-fields of the InAsSb/InAs lasers do not result from measurements artifacts or laser preparation, but rather from their intrinsic properties. Despite the unstable far-fields, the DH lasers showed excellent device characteristics (differential efficiency higher than 80%, J_{th} = 36 A/cm^2, and maximum output power about 3 W at 78 K).

Figure 13(b) shows far-fields of a MQW of structure A (see Table 2 for the detailed structures). Remarkably, the far-fields were found to be very stable for all operating conditions investigated. Up to 150 K and I = 2 A, the far-field of MQW lasers of structures A and B remained unchanged with the FWHM being 38° and 23°, respectively. As shown in Fig. 13(b), some distortion occurred in the far-field at high temperature operation (> 150 K); however, the FWHM remained unchanged. The narrower far-field of struc-

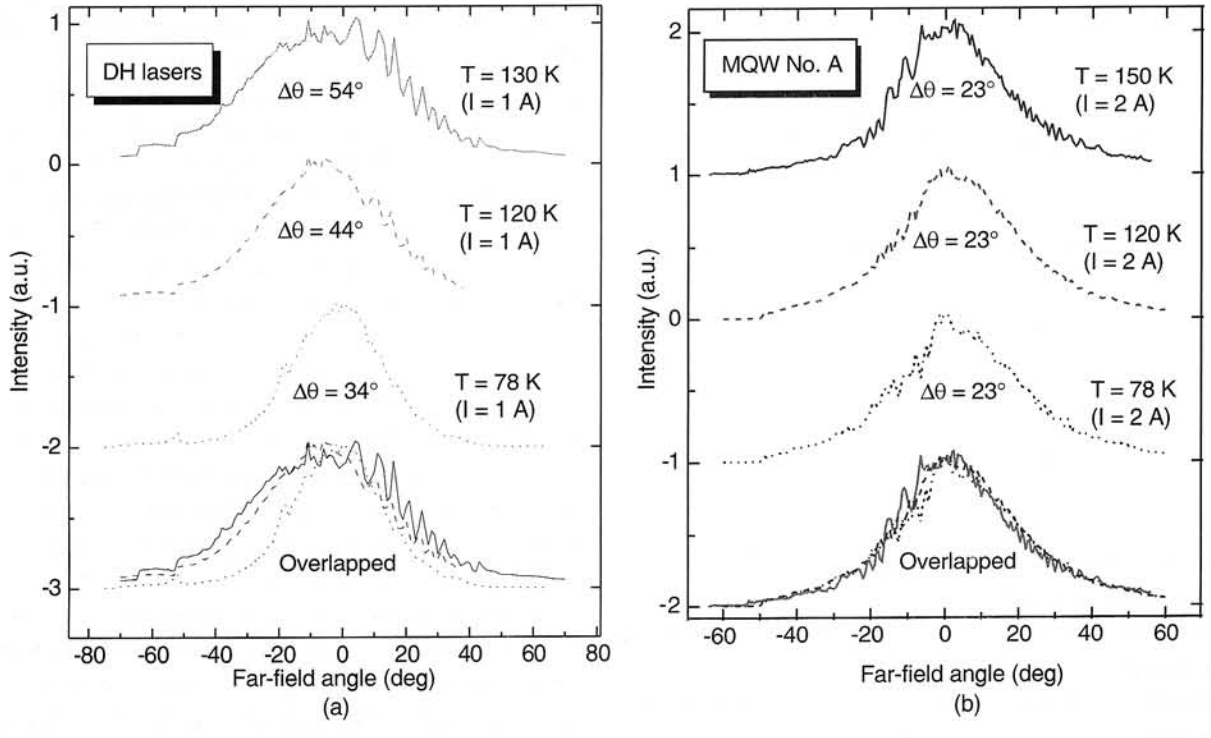

Fig. 13. Temperature and current dependence of InAsSb/InPAsSb/InAs (a) DH and (b) MQW lasers.

Table 2. Relevant device structures and characteristics. E_g, t, and, N_r represent the energy gap, thickness, and refractive index of the layer, respectively. $\Delta\theta$ is the FWHM of far-field in the direction perpendicular to the junction plane.

Structure	Active layer ($InAs_{1-x}Sb_x$)	Barrier (waveguide) layer	Cladding layer ($InP_xAs_ySb_{1-x-y}$)	$\Delta\theta$ (exper.)	$\Delta\theta$ (theory)
DH	t = 0.9 μm E_g = 388 meV N_r = 3.53	–	t = 1.5 μm E_g = 520 meV N_r = 3.42	34 ~ 54°	36°
MQW-A	t = 10 × 100 Å E_g = 344 meV N_r = 3.56	InAs E_g = 420 meV N_r = 3.52	t = 1.5 μm E_g = 520 meV N_r = 3.42	38°	38.5°
MQW-B	t = 10 × 100Å E_g = 344 meV N_r = 3.56	InPAsSb E_g = 460 meV N_r = 3.47	t = 1.5 μm E_g = 520 meV N_r = 3.42	23°	24°

ture B is due to the smaller refractive index difference between waveguide layer and cladding layer ($\Delta n \sim 0.05$) than in structure A ($\Delta n \sim 0.10$) [41]. The far-fields of MQW structures A and B coincide with the prediction of a conventional waveguide model where the transverse near-field optical distribution is obtained by directly solving Maxwell's equation in the DH and MQW structures, and then Fourier-transformed for the calculation of far-fields [42]. The calculated far-field FWHM's are in excellent agreement with experiment for the MQW lasers (see Table 2). However, the theoretical results for DH lasers have a significant discrepancy with the experiment, and cannot explain the instability of far-fields at high temperatures and/or currents.

In this subsection, we show that this behavior of far-fields in DH and MQW lasers can be explained from the refractive index fluctuation in the laser active region. First, the effect of the refractive index fluctuation on the far-fields in DH lasers is modeled below. The scattering of laser light due to the refractive index fluctuation can be obtained from Maxwell's equation; see equation (1). Since $\delta n \ll n$, we can expand **E** in a perturbation form and derive the scattered light: $\boldsymbol{E} = \sum_n E_n(z)\varphi_n(x,y)$ where $\varphi_n(x,y)$ decribes n^{th} optical mode of the cavity, and E_n decribes its amplitude as a function of the longitudinal direction z, and is given by

$$E_{n'}(z) \cong \frac{1}{2i\beta_{n'}} \sum_n \int_{z-l_n}^{z} dz' \exp[i\beta_{n'}(z-z')] C^2_{nn'}(z') \sim \frac{1}{2i\beta_{n'}} e^{i\beta_{n'} l_n} k_o^2 l_n \langle \delta n \rangle \quad (9)$$

where β_n is the longitudinal propagation constant of n^{th} mode, $C^2_{nn'}(z) \equiv nk_o^2 \int d\rho \phi_{n'}(\rho)\delta_n(\rho,z)\phi_n(\rho)$ and l_n is the absorption length of n^{th} mode [43]. It is important to note that l_n is generally much larger than the wavelength ($\sim 1/\beta_n$), and therefore the phases $\exp(i\beta_n l_n)$ in Eq. (9) can be considered random. It is this random nature that makes light scattered by the refractive index fluctuation have a distorted phase at the mirror facet. A calculated typical phase-front, i.e., the phase of $E_n(z)$ in Eq. (9), at the mirror is shown in Fig. 14(a) for a computer-generated random distribution $\delta n(r)$ with $\langle \delta n \rangle = 3 \times 10^{-4}$, 3×10^{-3}, and 10^{-2}, and a correlation length of about 100 nm. The first line of Eq. (9) was used for the numerical calculation. The phase front at the mirror is found to have a significant distortion ($\sim 0.5\pi$) for $\langle \delta n \rangle \sim 0.01$. When the phase of light is distorted, the far-fields are distorted accordingly, as predicted by the diffraction theory. The calculated far-fields are given in Fig. 14(b). (Detailed derivation of the scattered waves [Eq. (9)] and the effects on far-fields will be given elsewhere.) While detailed structure of the distortion of far-fields depends on a specific choice of distribution $\delta n(r)$ used for the calculation, amplitude and spatial frequency of the far-field were found to be practically independent of the selected $\delta n(r)$ for given $\langle \delta n \rangle$ and correlation length. The distortion (satellite peaks) and steering of the far-fields off the normal direction of the mirror are significant for $\langle \delta n \rangle \geq 0.01$. The distortion and steering of the far-fields at high temperature are consistent with experimental results in DH lasers at high operating temperatures [Fig. 13(a)]. The broadening of the far-fields at high temperatures is ascribed to an incoherent superposition of beams with different steering angles.

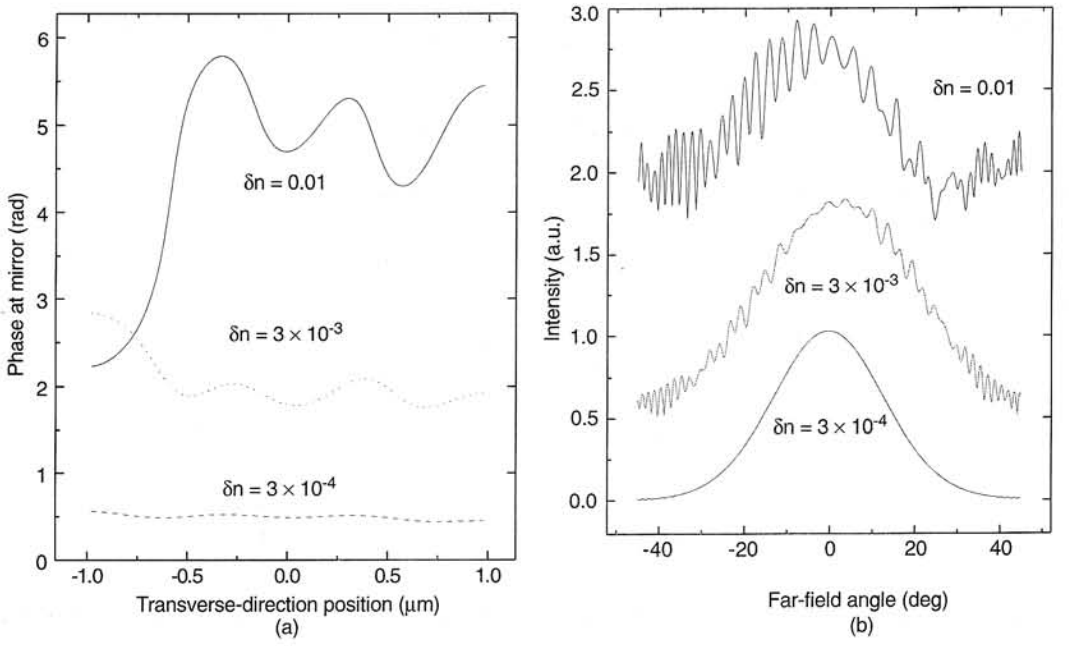

Fig. 14 Theoretical (a) phase-distortion and (b) far-field with refractive index fluctuation $<\delta n> = 3\times10^{-4}, 3\times10^{-3}, 10^{-2}$.

As discussed above, the refractive index fluctuation in the lasers results from the composition inhomogeniety, and the resultant non-uniform carrier distribution in the active layer. The increase in the refractive index fluctuation with temperature can be explained by the dependence of refractive index fluctuation on local temperature. (We believe that the effect of current on broadening of far-field is related to heating, and therefore has a similar origin as the effect of temperature). Refractive index in semiconductor is known to be very sensitive to temperature when the wavelength of light is close to energy gap [44], as in the present case, and thus local temperature fluctuation can significantly increase δn. Since free-carrier absorption is the dominant mechanism of the optical loss in midwave-infrared wavelength, and its magnitude increases rapidly with an increase in temperature [45], it is expected that the non-uniform carrier distribution in the material leads to a large increase in temperature fluctuation and, as a consequence, refractive index fluctuation as temperature increases. Similarly non-radiative recombinations with strong temperature dependence such as Auger recombination or surface recombination can also result in the local temperature fluctuation because of the non-uniform carrier distribution.

The MQW structure is expected to have a much smaller degree of refractive index fluctuation. It is because first the total volume of the active region of MQW structure (10×100 Å) is about 10 times smaller than that of DH structure (~1 μm). Thus the effect of non-uniform carrier distribution in the active region on the total refractive index should be much smaller for this structure. Furthermore, the carrier distribution within the quantum wells is uniform in the growth direction because well width (100 Å) is smaller than the characteristic length of composition inhomogeneity (~100 nm). Therefore it can be assured that carrier distribution is much more uniform (or regular) in MQW structure than in DH structures. This much higher uniformity (or regularity) of carrier- and refractive-index-distributions and the relatively small effect of active region on the total refractive index in MQW structure, therefore much smaller n, are consistent with the stable far-fields in our MQW lasers [Fig. 13(b)].

2.3.3. Threshold current of short–cavity lasers

The composition inhomogeneity also significantly affects the threshold current of the lasers. The cavity length dependence of threshold current density of typical InAsSb/InPAsSb DH lasers are shown in Fig. 15. Rather rapid increase of J_{th} was observed with the decrease of cavity length. In order to understand this behavior, we have compared these experimental results with theoretical predictions. The dotted line represents the theoretical result obtained using a standard radiative recombination model based on Kane's Hamiltonian for calculation of the material gain and threshold current density as a function of cavity length

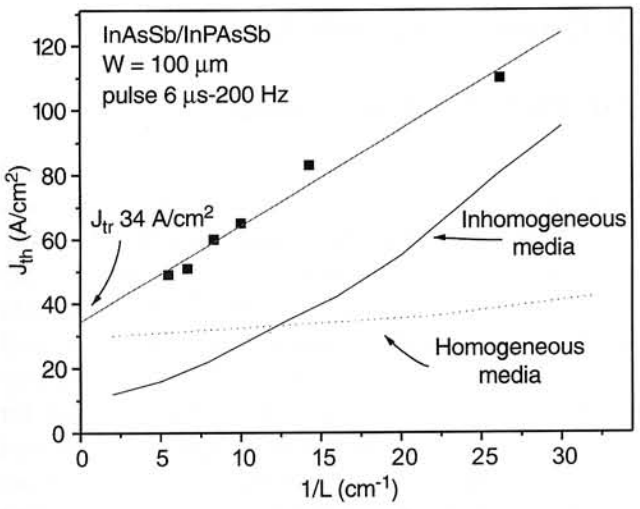

Fig. 15. Threshold current density vs inverse cavity length for 100 μm-wide InAsSbP/InAsSb/InAs DH lasers at 77 K.

[46]. In this calculation, InAsSb active layer is assumed to forming a single-phase alloy with a homogeneous composition. The Auger recombination and minority-carrier leakage current are not included in this calculation as they are negligible in this temperature range (~ 90 K). In this calculation, it was found that the theoretical J_{th} does not significantly depend on the cavity length (Fig. 15, dotted line) and thus cannot explain the strong cavity length dependence of J_{th} observed in experiment. Small increase of the theoretical values of J_{th} for the decrease in cavity length (i.e. an increase in the mirror loss) is attributed to high differential gain (a rapid increase of the material gain g with an increase of the carrier density n) in this model (Fig. 16) that assumes homogeneous composition.

In order to understand the effect of the inhomogeneity of InAsSb active layer alloys on the threshold current of lasers, we perform a new calculation with including the composition inhomogeneity effect. To incorporate the effect of composition inhomogeneity, we used a simple model for inhomogeneous gain media: we assumed that the semiconductor alloy in the active region has several phases with different energy gaps due to different composition, and thus has different gain spectra. The average material gain spectrum was obtained by averaging the gain spectra of these regions

$$G(\omega) = \sum_i \gamma_i G_i(\omega) \qquad (10)$$

where i denotes the region with a different composition, γ_i is the fractional volume of i^{th} region, and $G_i(\omega)$ is the optical gain spectrum of the i^{th} region. The energy gap fluctuation ΔE_g was assumed to be about 30 meV, what corresponds to the photoluminescence spectrum width measured at 78 K [47]. While broadening of spectrum is also caused by scattering of carriers by, e.g., phonons or other carriers, it is unlikely that these mechanisms significantly contribute to the PL width at low temperature. The energy gap at each region is determined from Gaussian distribution with ΔE_g for its standard deviation. The spectrum of radiative recombination $R(\omega)$ was similarly calculated by summing $R_i(\omega)$ at each region i with different energy gap. The solid line in Fig. 15 represents the result of the new model. Strong gain saturation in the inhomogeneous-composition material results in rapid increase of J_{th} with a decrease of a cavity length, as consistent with experiment. The gain saturation results from the formation of microscopic smaller energy-gap regions that act like quantum well. Since the regions have very shallow energy barrier (DEg ≈ 30 meV), "carrier spillover" will be very significant, making such a strong gain saturation. Due to unknown material parameters of the InAsSb alloys, quantitatively accurate modeling is inhibited, resulting in some discrepancy shown in Fig. 15. Nevertheless, the above results indicate that the inhomogeneity of the materials is significant and may be the governing factor that inhibits laser performances at high temperatures. The reasonably good agreement between experiment and theory suggests that our assumption of the small non-radiative recombination (Auger recombination and leakage current) is valid, and furthermore other non-radiative recombinations through Shockley-Reed impurity level are not significant.

2.4. Future works

Although the current results from the InAsSbP material system show a great potential for laser diodes emitting in the 3 to 5 μm range, further increasing the wavelength is restricted by the large mismatch between the quantum well and barriers. This will dramatically degrade the structure optical quality when $\lambda > 5$ μm. Therefore, the alternative system, such as type II and QCL which will be discussed in the following sections, should be considered in order to extend the wavelength into long-infrared region.

Another problem of the low band gap materials are their susceptibility to the even small amount of bulk- and interface-defects, degrading the function of pn junction, due to e.g. impurity-assisted-tunneling. The much softer low band gap materials compared to higher band materials has relatively lower

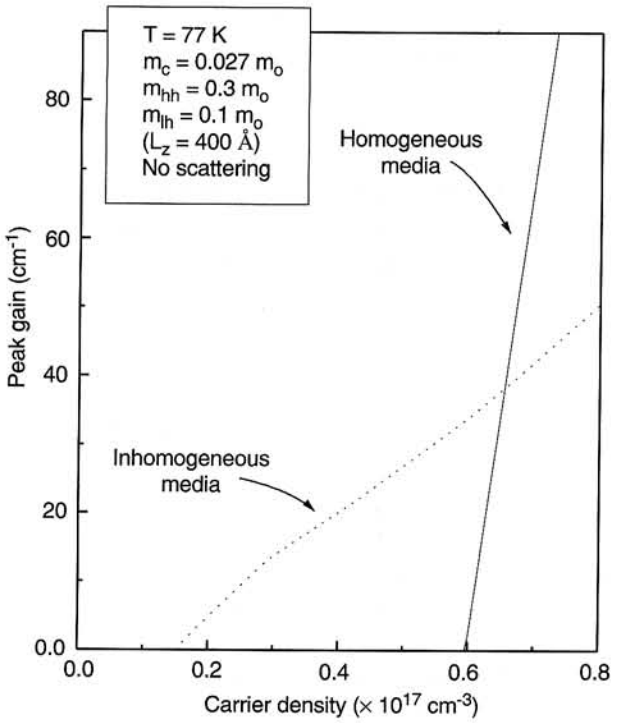

Fig. 16. Calculated peak gain vs injection carrier density N of InAsSb/InPAsSb DH lasers. Solid line: when it is assumed that the lasers have spatially homogeneous composition. Dotted line; when it is assumed that the lasers have spatially inhomogeneous composition.

thermal conductivity, making the heat-dissipation the major issue in device design. We also discussed the "anomaly" in optical properties (far-field, cavity resonance frequencies) in InAsSb alloys, which may limit material combination for the heterostructure lasers.

Nevertheless, the rapid improvement of the material quality in the InAsSbP system in recent years indicates that even higher material quality can be expected with further optimization of the growth conditions. Consequently, the optimization of the growth conditions of the InAsSbP will remain still the major factor that determines laser performance in future. More sophisticated structures should be designed and fabricated to give higher carrier and optical confinement. This will reduce the leakage current and lower the internal loss so that sufficient gain can been attained for lasers to be operated at a higher power and at a higher operation temperature. Finally, proper strain should be incorporated into QWs, as some of preliminary calculation predicted that strain may suppress Auger recombination which is considered to be the major physical mechanism that limits high temperature operation of this type of lasers.

3. Quantum cascade lasers

3.1. Historical background

The idea of generating light from intersubband transitions within semiconductor quantum wells was first proposed by Kazarinov and Suris in 1971 [48]. Since then, many groups have tried to produce devices based on similar models. However, due mainly to immature growth technology and lack of physical understanding of the nonradiative relaxation mechanisms, no useful prototypes were demonstrated for many years. The turning point began when the first electrically pumped intersubband laser at $\lambda = 4.2$ μm was demonstrated in 1994 [16]. This laser, dubbed the "quantum cascade laser", was evidence of a remarkable design taking advantage of both a three- -level laser design and semiconductor band-gap engineering.

This AlInAs/GaInAs-based device grown by molecular beam epitaxy (MBE) has since undergone a series of changes that have led to long-wavelength emission, high temperature pulsed operation, and demonstration of a single longitudinal mode DFB design [49,50]. Continuing research in other groups has shown that the quantum cascade laser (QCL) is repeatable using other growth techniques such as gas-source molecular beam epitaxy (GSMBE) [51]. Also, the same design was utilized for the GaAs/AlGaAs material system, which gave electroluminescence at 6.9 μm [52]. The high temperature (>300 K) pulsed operation, high power (>1 W peak at 77 K) capabilities, and tunable emission wavelength make the QCL attractive for many applications in the 3–12 μm infrared range. In the following subsections, the various aspects of the QCL will be explored along with its current limitations.

3.2. Advantages of the quantum cascade laser

The most important advantage of the quantum cascade laser is its insensitivity to temperature changes. Laser operation is not limited by Auger recombination due to the unipolar nature of the device, which gives a much higher theoretical operating temperature. This high temperature operation potentially will reduce package size and cost due to the absence of elaborate cooling systems. More significant advantage of QCL is that relatively mature InP or GaAs technology is used. This ensures that growth and other physical characteristics of the materials are rela-

tively well understood for QCL, compared to interband-type counterpart that use InAs or even more exotic InGaAsSb systems which are far more difficult to grow with physical properties much less understood.

The tunability of the emission wavelength is also a serious advantage to the QCL design. Interband systems tend to rely on different material stoichiometries to achieve longer emission wavelengths. This can result in new growth and processing steps. The QCL emission wavelength is controlled solely by layer thickness and makes use of mature InP growth technology that leads to higher uniformity at lower per wafer cost. Lastly, the cascade, or serial, nature of the active region stack has been designed to emit more than one photon per electron above threshold. Typically, 25–30 periods are used, which can result in a differential efficiency as high as $\eta_d = 4.78\%$ and $\lambda \sim 5$ μm.

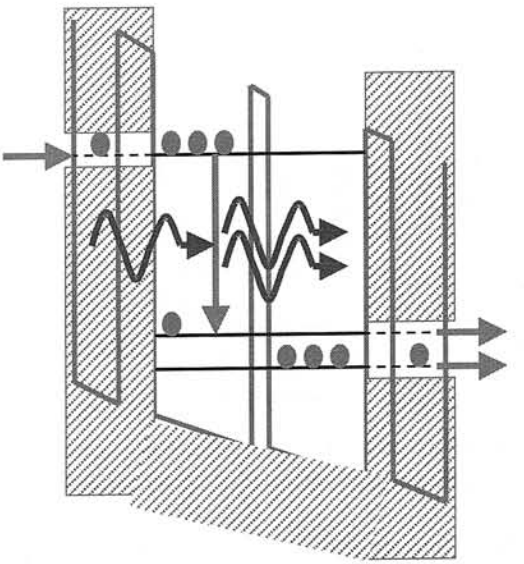

Fig. 17. Example of quantum well-based active region for electrically injected quantum cascade laser.

3.3. Physics and design principles

Unlike the interband lasers, which have bipolar device characteristics, relying on electron-hole recombination to generate light, the QCL is a unipolar device, which use only conduction-band electrons. Semiconductor quantum wells have the property of splitting bulk band structure into a series of subbands. When electrons move between these subbands, they undergo changes in their energy and/or momentum as would be expected. However, the main difference between an intersubband laser in the conduction band and an interband laser is the fact that all subbands have an equal sign (positive) for their effective mass. This means that the electron is the dominant carrier and that emitted light is solely due to electrons relaxing from upper to lower subbands. The benefit of this design is that, using the same material, the emission energy can be varied over a wide range (limited by the conduction band offset between the barrier and well) simply by varying the well widths.

In order to have stimulated emission, there has to be a population inversion. This means that there must be a steady injection of high-energy electrons and steady collection of low energy electrons from the same quantum well region. For an efficient injection of high-energy "hot" electrons into the active region, a special injector region was designed which connects two adjacent active regions. This injector is a complex energy filter in which quantum mechanical tunneling and phonon-assisted tunneling can draw low energy electrons from one active region and supply them as high energy electrons to the next. A schematic of how this can be used to connect many active regions in series is shown in Fig. 17. The relaxation rate from the 2nd subband to the 1st is very quick due to the energy spacing being close to resonance with the optical phonon energy. These two designed features of the QCL ensure a population inversion between the 2nd and 3rd levels, assuming their energy difference is greater than the optical phonon energy.

In order to establish energy lineup and electron distribution among adjacent layers, we need a very specific device design and the corresponding electric field. The current active region of the QCL is a triple AlInAs/GaInAs quantum well structure that supports three subbands as illustrated above. The injector region is made up of the same material and has four or more wells depending on the emission wavelength. Solutions to Schrödinger's equation using the proper energy-dependent effective mass give very good estimates of the allowed wavefunctions and energy levels in the laser structure. The equation used is given as:

$$\frac{\hbar^2}{2}\frac{d}{dz}\left(\frac{1}{m^*(E,z)}\frac{d\Psi}{dz}\right)+\left(E-V(z)-\frac{\hbar^2 k_t^2}{2m^*(E,z)}\right)\Psi=0 \quad (11)$$

where Ψ is the electron wavefunction, V(z) is the heterostructure potential profile, $m^*(E, z)$ is the energy dependent effective mass, and k_t is the in-plane momentum.

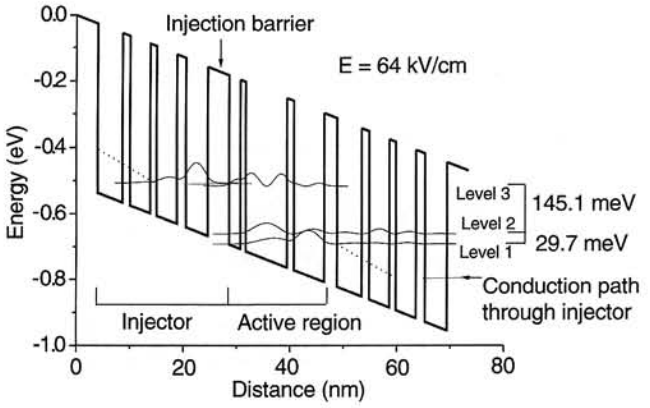

Fig. 18. Conduction band profiles for a type I quantum cascade active region surrounded by two injectors.

One solution for λ = 8.5 μm laser structure is shown in Fig. 18 under an electric field of 64 kV/cm. Only the modulus squared of the central wavefunctions are shown. The coupling between the wavefunctions in the active and injector regions is apparent, as well as the predicted emission energy of 145.1 meV, or 8.546 μm. The waveguide design for long-wavelength lasers is also crucially important. Free carrier absorption scales as λ^{2-3}, and the refractive index also changes rapidly as doping increases at longer wavelengths. Experimental measurements of the waveguide loss have been reported as 13.3 cm^{-1} at 5.1 μm and 34 cm^{-1} at 8.5 μm. Due to quantum mechanical selection rules, the light emitted from a QCL is inherently TM in nature. In other words, the light is polarized in the direction of quantization. An example of the index profile and fundamental TM mode for an 8.5-μm laser structure is shown in Fig. 19.

3.4. Device performance

The excellent performance demonstrated thus fa by QCL technology gives us a hint at its developec potential. Shown below in Fig. 20 are the output char acteristics for an 8.5 μm QCL in pulsed operation The QCL shown here is a gas-source MBI AlInAs/GaInAs triple QW QCL [51]. The QCL is the first semiconductor laser to operate in the mid- and far-infrared at room temperature with high peak powers (>25 mW). Also, the low sensitivity to temperature changes is evidenced by the high T_0 values [51].

An updated summary of the reported results for QCLs is shown in Fig. 21. Room temperature pulsed mode operation has been demonstrated at both $\lambda \sim 5$ μm and $\lambda \sim 8.5$ μm. On the shorter wavelength side, strain-compensating growth techniques produced a laser at λ = 3.4 μm that operated in pulsed mode up to 280 K [53]. However, yet the continuous wave (cw) operation demonstrated thus far takes place only at significantly lower temperatures. High temperature cw operation (T ~ 110 K) has only been reported at $\lambda \sim 5$ and 8.5 μm. Increasing the CW operating temperature is one of the main challenges to be addressed for the QCL.

3.5. Future works

The quantum cascade laser is still a relatively new technology (~ 4 years). The devices currently being developed show very nice characteristics and have no real competition among semiconductor lasers in terms of output power and pulsed operating temperatures

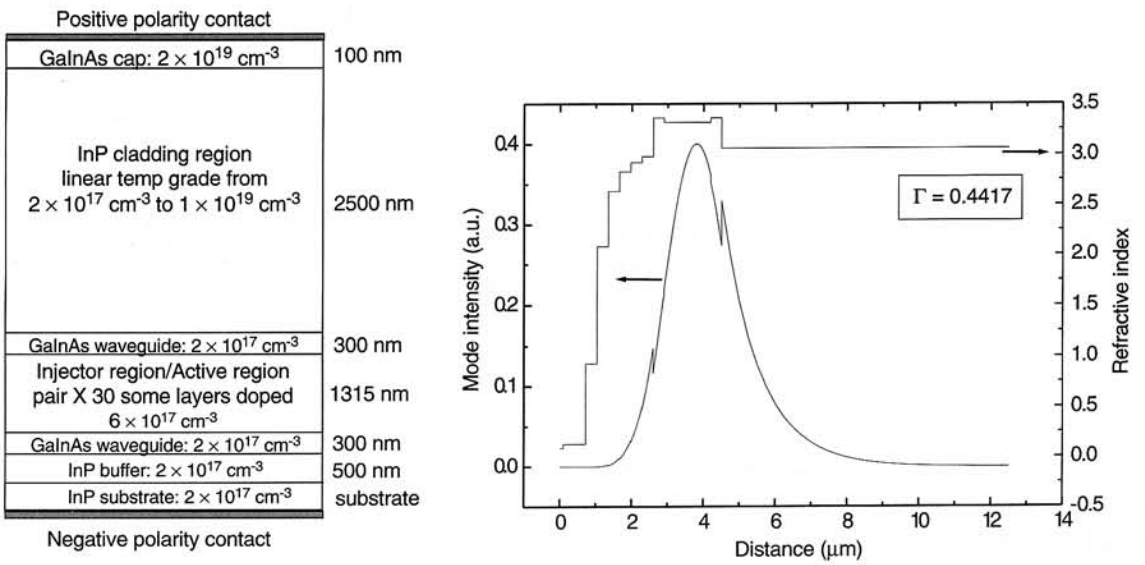

Fig. 19. Cross-section of QCL laser structure and fundamental TM mode with confinement factor.

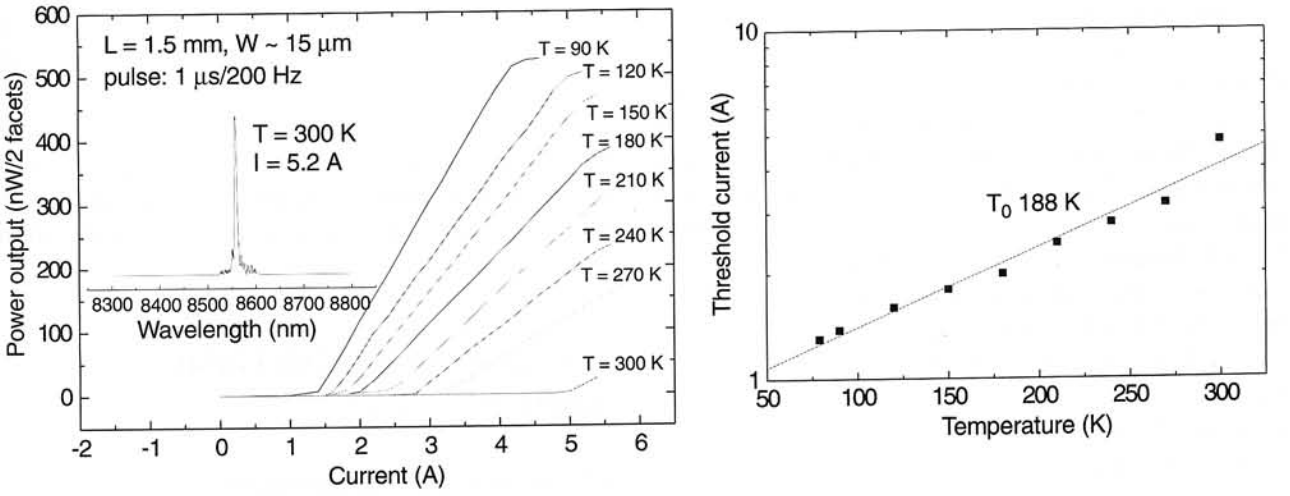

Fig. 20. Sample output characteristics of an 8.5 μm quantum cascade laser.

for $\lambda > 5$ μm. Of significant interest is the development of this technology specifically for the 5–12 μm range. However, due to some of the limitations mentioned below, improvements need to be made in a number of areas.

Along with the advantages shown by the QCL, there are also some physical limitations to the device performance. Because the population inversion is mainly due to differences in the polar optical phonon scattering rates between subbands, as the emission energy becomes closer to the optical phonon energy, the threshold current requirement increases rapidly. This places significant restriction on the long (>20 μm) emission wavelengths. Current emission wavelength up to 17 μm has been demonstrated at low temperature [54].

As for the short wavelength limit, the heterostructure conduction band offset is the deciding factor; the 2nd to 3rd subband energy spacing can never be higher than the total barrier height. In order to overcome this, strain-compensating epitaxy of AlInAs/GaInAs has been used to increase the barrier height as mentioned above. Heterostructures with higher band offsets such as InAs/AlSb heterostructures have been recently proposed, but they have not yet been made in practice due to difficulty of material growth. These structures may also suffer from intervalley scattering problems.

Free carrier absorption can also play an important role in implementation of electrically-injected long wavelength lasers. Just like any other laser there is a trade-off between an electrically conducting laser structure (less heating) and a low waveguide loss la-

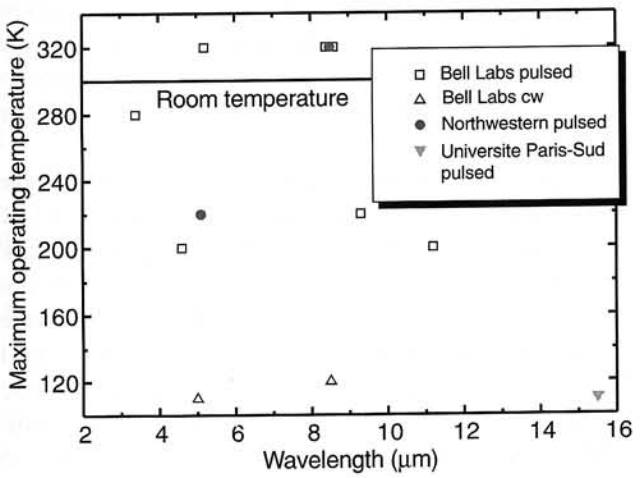

Fig. 21. Summary of results for type I quantum cascade lasers.

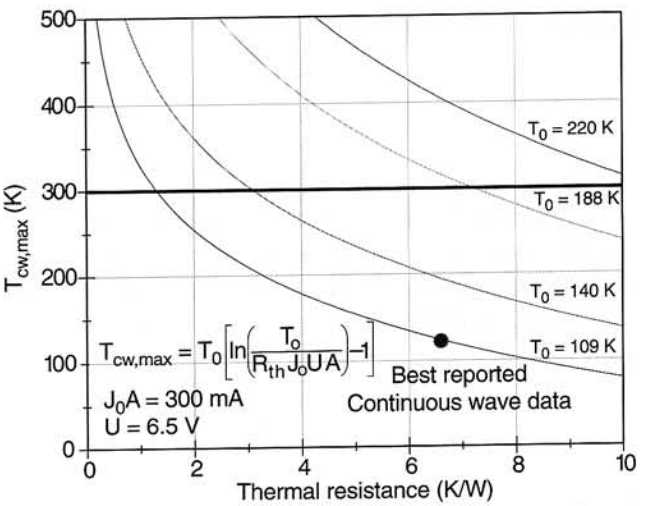

Fig. 22. Theoretical predictions for the maximum cw operating temperature as compared to experimental results.

ser (lower threshold condition). This is a major problem in the QCL for two reasons. First, the free-carrier absorption coefficient is very large for even moderate doping in the mid-infrared, and secondly, the TM mode spreads farther into the cladding for longer wavelengths. This trend may produce prohibitively thick epilayers and higher voltage operation for longer wavelengths. Despite the technical difficulty associated with precisely controlled thin film growth has been much eased in many aspects through past several years of intensive study on InGaAs/AlGaAs systems, the QCL is still very complex and requires many hundreds of layers.

Another important issue in QCL is the low wall-plug efficiency and high power requirements of the lasers. At low temperatures (~ 22 K), a very good wall-plug efficiency of 8.5% has been demonstrated, but the efficiency drops off quickly as the temperature is raised. At 80 K, it is less than a third as much. Also, the voltage and current requirements are significant at high temperatures even in pulsed mode. While threshold current densities are around 1–2 kA/cm^2 at low temperatures, they increase up to around 9–10 kA/cm^2 at 300 K. This requires pulses of >3 A of current at ~ 6.5 V.

Currently, no cw lasing has been reported over 120 K, what is believed to result from low wall-plug efficiency that causes significant device heating. This would still require the use of expensive multi-stage coolers, which is undesirable in many practical applications. The maximum cw operating temperature is related to many physical parameters such as characteristic temperature T_o, thermal resistance of the laser, and the operating voltage. When threshold current is expressed as a function of temperature

$$J_{th} = J_o \exp\left(\frac{T}{T_o}\right) \tag{12}$$

where J_o and T_o are the fitting parameters in A/cm^2 and K, respectively, a simple equation can be derived to estimate the maximum cw operating temperature assuming a linear thermal resistance for the device as [55]

$$T_{cw,\max} = T_o\left[\ln\left(\frac{T_o}{R_{th}J_o UA}\right) - 1\right] \tag{13}$$

where R_{th} is the thermal resistance of the laser, U is the operating voltage, and A is the stripe area. This equation is plotted in Fig. 22 vs. R_{th} for several values of T_o. Also plotted is experimental data gathered for a 5-μm QCL. Decreasing R_{th} and increasing T_o should raise the maximum temperature of this device significantly. This will be most likely accomplished through further refinements in the material quality, device structure, and heat sinking arrangement.

4. Type II InAs/AlSb/GaSb superlattice lasers

4.1. Historical background

Type II band alignment and some of its interesting physical behaviors were originally suggested by Sai-Halasz and Esaki [56] in 1977. Experimentally the optical absorption of type II superlattices [57] and later the semimetal behavior of the superlattice [58] were reported shortly after the theoretical prediction. The applications of such superlattices to electronic and optical devices were proposed several years later [59], such as resonant tunneling diodes RTD and hot electron transistors. This novel type of superlattice provides a very flexible "effective energy gap" and when used for optoelectronic devices such as lasers or detectors, can cover a wide infrared range (2 to > 50 μm). On the contrary, emission wavelength longer than 5 μm are virtually impossible for Sb-based type I interband lasers because of lack of suitable lattice-matching material system. Furthermore, it was theoretically predicted that type II superlattice structure may have significantly suppressed Auger recombination rate, which is widely argued to be the major intrinsic physical mechanism that limits high-temperature operation of type I interband mid-infrared lasers [60]. Many impressive results have been achieved recently in type II modulators [61], detectors [62], and laser diodes [14,15].

Type II bipolar and unipolar (cascade) lasers have shown impressive performance. T_o as high as 81 K was obtained up to T_{max} = 170 K from InAs/GaInSb/AlSb type II bipolar cascade lasers for λ = 3.85 μm with J_{th} = 290 A/cm^2 at 80 K [63]. High temperature performance, however, is yet to be seen. Like type I Sb-based lasers, the difficulty still remains the precise control of material growth, particularly reproducibility of cascaded QW regions. Presumably due to this reason, so far high power operation is not as good as type I Sb-based lasers.

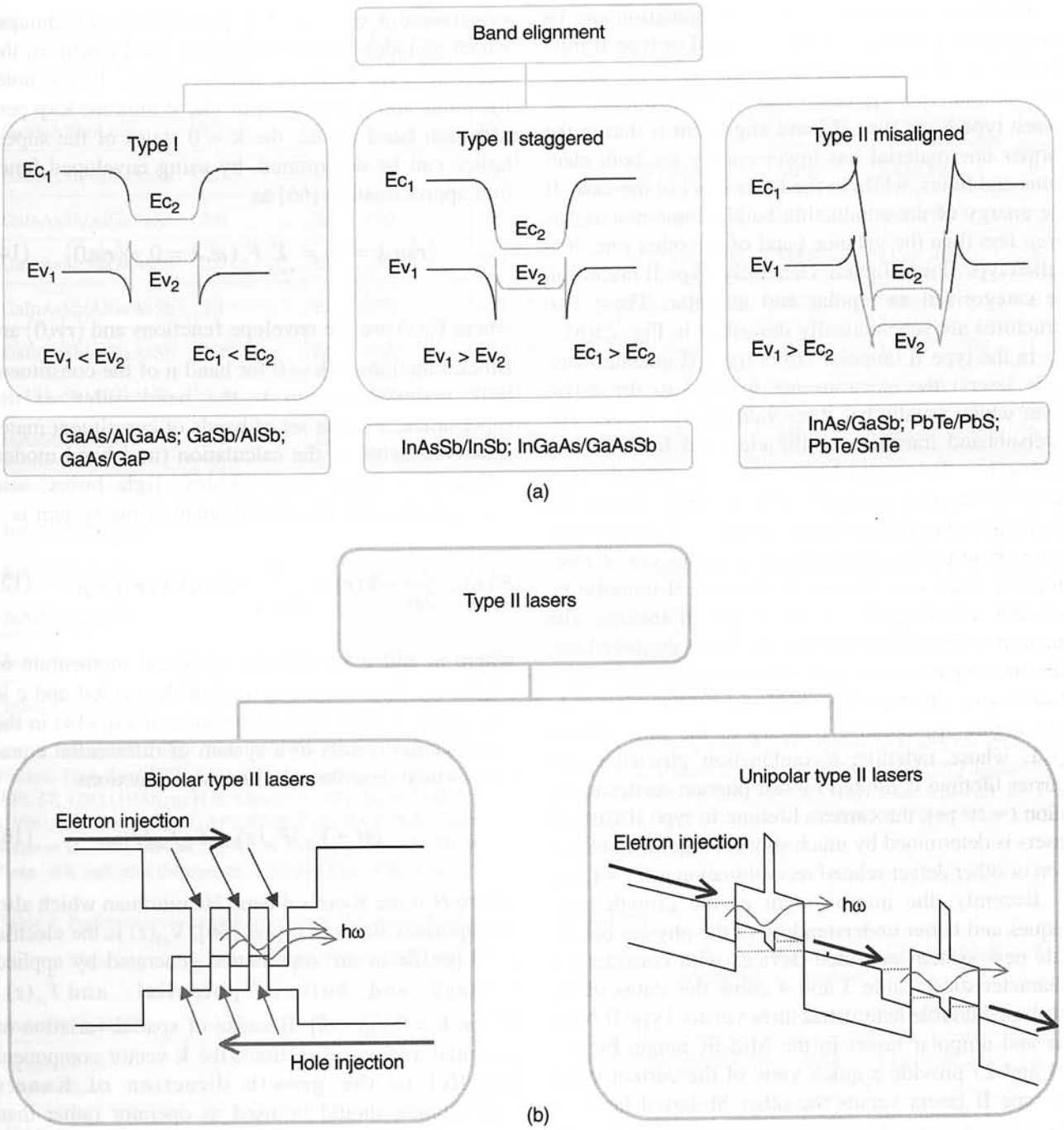

Fig. 23. (a) Band alignment of type I, type II staggered and type II misaligned; (b) type II bipolar and unipolar laser structures.

4.2. Fundamental operation principle

4.2.1. The band alignment

Most of the mid-infrared applications need diode lasers with high output power and near room temperature operation. Unfortunately, the usual technology for visible and short infrared lasers has not been successful in achieving the above needs in the mid-infrared range. It has been proposed [64] that type II laser diodes may provide higher performance in the mid-infrared range because of their lower Auger recombination rate, lower threshold current and higher characteristic temperature, T_o, than GaInAsSb and HgCdTe lasers [65]. The lasing wavelength of type II lasers can be adjusted to a wide range, by simply changing the thickness of the layers, so the growth reproducibility is better than the structures that use quaternaries like GaInAsSb, AlGaAsSb or AlInAsSb layers.

The band alignment of any heterojunction can be categorized as type I, type II staggered or type II misaligned, as illustrated in Fig. 23(a) with a few examples of material systems. The main difference between type I and type II band alignment is that in the former one material has lower energy for both electrons and holes, while in the latter it is not the case. If the energy of the conduction band of one material is even less than the valance band of the other one, it is called type II misaligned. Generally Type II lasers can be categorized as bipolar and unipolar. These two structures are schematically described in Fig. 23(b).

In the type II unipolar lasers (type II quantum cascade lasers) the electrons are injected to the active layer which usually has three valid energy levels. The intersubband transition of the electrons from the top subband to the second band causes the optical radiation. The electrons, which have lost energy during this intersubband transition, however, are re-used in generating photons over again. Because of this use of electrons in multi-stage transition, the type II unipolar lasers are called type II cascade lasers, in analogy with the intersubband quantum cascade lasers discussed earlier. In comparison to type I intersubband quantum cascade lasers, this type II cascade lasers have lower J_{th} and higher η_d, because contrary to the intersubband QCL whose radiative recombination efficiency and carrier lifetime is limited by fast phonon carrier relaxation (~ 10 ps), the carriers lifetime in type II cascade lasers is determined by much slower Auger recombination or other defect-related recombination rate (~ 1 ns).

Recently, the improvement of the growth techniques and better understanding of the physics behind this new system provided devices with considerable characteristics. Table 3 and 4 show the status of the Sb-based double heterostructures versus Type II bipolar and unipolar lasers in the Mid-IR range. Figures 24 and 25 provide a quick view of the current status of type II lasers versus the other Sb-based lasers in the Mid-IR range. Results summarized in Table 5 are the best reported in literature of mid to long wavelength lasers between λ = 3 μm to 12 μm.

4.2.2. Type II lasers

In the type II bipolar lasers the structure of a III–V laser diode is used except that the active layer is a type II superlattice and the transition is between the C1, the first conduction miniband, and HH1, the first heavy-hole miniband. Unlike to QCL which considers only conduction-band electrons, the miniband energy profiles in the active layers can be calculated using a superlattice 8 or 4 band **k**×**p** perturbation technique which includes lowest conduction-band electrons, the uppermost six pairs of valance bands: heavy hole, light hole and spin-orbit split-off. Within the **k**×**p** perturbation band model, the **k** = 0 states of the superlattice can be determined, by using enveloped function approximation [66] as

$$\langle \boldsymbol{r}|m,\boldsymbol{k}=0\rangle = \sum_{n\in S} F_n(m,\boldsymbol{k}=0,z)\langle \boldsymbol{r}|n,0\rangle \qquad (14)$$

where $F_n(z)$ are the envelope functions and $\langle \boldsymbol{r}|n,0\rangle$ are Block functions at **k** = 0 for band n of the constituent bulk material and m is the band index of the superlattice. S is the set of bands of constituent materials considered in the calculation (in 4 band model, conduction band, heavy-holes, light-holes, and spin-split bands). The Hamiltonian of the system is

$$H(\boldsymbol{r}) = \frac{p^2}{2m} + V(\boldsymbol{r}) + \frac{\hbar}{4m^2c^2}[\sigma \times \nabla V(\boldsymbol{r})] \times p \qquad (15)$$

where m and p are the free mass and momentum of electrons, V(**r**) is the potential of the crystal and c is the speed of light. The substitution of Eq. (14) in the Hamiltonian results in a system of differential equations which describes the envelope functions

$$(\hat{H} + V_{el})\hat{F}_m(z) = E_m \hat{F}_m(z) \qquad (16)$$

where $\hat{H}$ is the Kane's 4 band Hamiltonian which also incorporates strain in layers [66], $V_{el}(z)$ is the electric field profile in the superlattice generated by applied voltage and built-in potential, and $\hat{F}_m(z) = [F_n(m,\boldsymbol{k}=0,z)|n \in S]$. Because of spatial variation of potential and wavefunctions, the **k** vector component parallel to the growth direction of Kane's Hamiltonian should be used as operator rather than constant as

$$p_z = -i\frac{h}{2\pi} \times \frac{\partial}{\partial z} \qquad (17)$$

For an infinite superlattice with the two alternating layers of thickness of a (layer 1) and b (layer 2), the Eq. (16) can be analytically solved, yielding E–k dispersion relation as

$$\cos[q(a+b)] = \cos(k_1 a)\cos(k_2 b) - \frac{1}{2}\left(\frac{k_1\mu_2}{k_2\mu_1} + \frac{k_2\mu_1}{k_1\mu_2}\right)\sin(k_1 a)\sin(k_2 b) \qquad (18)$$

Table 3. Performance comparison of Sb-based DH laser diodes reported in the literature.

Material	Wavelength (μm)	Pump	Diff. effic. (%)	T_{max} (K)	T_o (K)	P_{max} (mW)@(K)	Growth method	J_{th}[A/cm^2]@(K)	Ref.
GaSb/AlGaAsSb	1.73	El	–	300	–	–	MOCVD	2.1×10^3@300	a
GaInAsSb/AlGaAsSb	2.0	El	23	300	–	750 cw@300	MBE	330@300	b
GaInAsSb/AlGaAsSb	2.0	El	70	300	70	1300 cw@300	MBE	143@300	c
GaInAsSb/AlGaAsSb	2.0	El	53	300	–	1900 cw@300	MBE	115@300	d
GaInAsSb/AlGaAsSb	2.1	El	70	450	113	190 cw@300	MBE	260@300	e
GaInAsSb/AlGaAsSb	2.29	El	18	300	50	250 cw@300	MBE	1.7×10^3@300	f
GaInAsSb/AlGaAsSb	2. 9	El	0.5	255	28	45 cw@300	MBE	80@100	g
InAsSb/AlAsSb	3.9	El	–	105	20	30 cw@70	MBE	18@40	h
InAsSb/InAlAsSb	3.5	El	–	175	35	30 cw@80	MBE	30@77	i
InAsSb/InAlAsSb	3.9	El	–	165	30	–	MBE	78@77	j
InAsSb/InAsSbP	3.5	El	–	130	33	33 pulse@77	MOCVD	250@7	k
InAsSb/InAsSbP	3.6	El	–	100	23	10 cw@100K	LPE	1.4×10^3@100	l
InAsSb/InGaAs	3.6	El	0.06	100	–	30 pulse@77	MOCVD	100 @77	m
InSb/AlInSb	5.1	El	–	90	16	28 pulse@77	MBE	1480 @77	n

a) C.A. Wang et al., Elect. Lett. **32**, 1779 (1996); b) H.K. Choi et al., IEEE Photonic Tech. Lett. **5**, 1117 (1993); c) H.K. Choi et al., IEEE Photon. Tech. Lett. **PTL-6**, 7 (1994); d) Garbuzov et al., APL **70**, 2931 (1997); e) K. Choi et al., APL **61**, 1154 (1992); f) S.J. Eglash et al., APL **57**, 1292 (1990); g) H.K. Choi et al, APL **64**, 2474 (1994); h) H.K. Choi et al, APL **65**, 2251 (1994); i) H.K. Choi et al, APL **68**, 2936 (1996); j) H.K. Choi et al, APL **67**, 332 (1995); k) S.R. Kurtz et al., APL **68**, 1332 (1996); l) Popov et al., APL **68**, 2790 (1996); m) S.R. Kurtz et al., APL **64**, 812 (1994); n) Ashley et al., APL **70**, 931 (1997).
Note: @K indicates the operation temperature of the lasers.

Table 4. Performance comparison of type II laser diodes reported in the literature.

Material	Wavelength (μm)	Pump	Diff. effic. (%)	T_{max} (K)	T_o (K)	P_{max} (mW)@(K)	Growth method	J_{th}[A/cm^2]@(K)	Ref.
InAs/GaSb MQW	2.32	El	30	300	90	–	MBE	7.9×10^3 @300	o
InAs/GaInSb Superlattice	2.9	El	15	260	33	800 pulse@100	MBE	1.1×10^3 @200	p
InAs/GaInSb VCSEL	2.9	Op	1(at 200K)	280	34	2000 pulse@260	MBE	10^3 kW* @280	q
InAs/GaInSb "W" Quantum Cascade	3.0	El	–	225	53	430 pulse@100	MBE	2.5×10^3 @220	r
InAs/GaInSb/AlSb Quantum Cascade	3.85	El	131	170	81	500 pulse@80	MBE	290@80	s
InAs/GaInSb/GaInAsSb Superlattices	3.8	El	–	84	30	1-2 pulse@80	MBE	407@80	t
InAs/GaInSb/InAs/AlSb MQW	4.5	Op	0.2	310	41	2000 pulse@200	MBE	100 kW* @300	u

o) A.N. Baranow et al, APL **71**, 735 (197); p) W.W. Bewley et al, submitted to APL; q) C.L. Felix et al, submitted to APL; r) C.L. Felix et al, submitted to Photon. Tech. Lett.; s) R.Q. Yang et al., APL **71**, 2409 (1997); t) A.R. Kost et al., SPIE **2382**, 271 (1995); u) C.L. Felix, Photon. Tech. Lett. **9**, (1997).
Note: * The lasers are optically pumped so that their threshold is in the unit of W/cm^2.

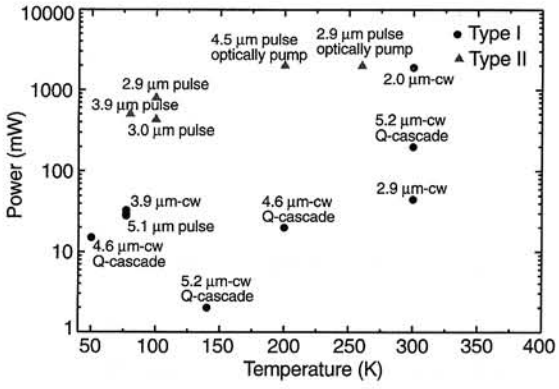

Fig. 24. Maximum power vs operating temperature for various types of mid-infrared lasers.

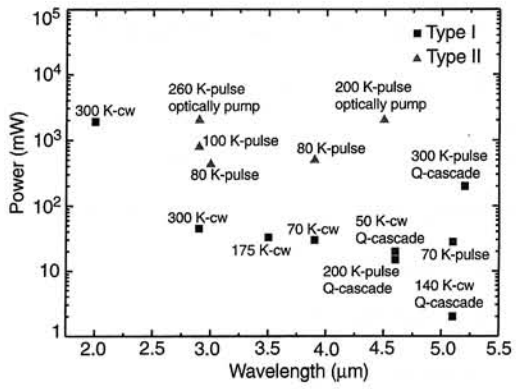

Fig. 25. Maximum power vs emission wavelengths for various types of mid-infrared lasers.

Table 5. The best results for injection mid-infrared type I, type II, quantum cascade lasers.

Type I interband lasers

Material	λ (μm)	Max. pulse (cw) operating temperature (K)	Max. pulse (cw) power (mW)	T_o(K)	J_{th} (A/cm^2) at 78 K	η_d (%) at 78 K	Growth method	Ref.
InAsSb/InAlAsSb	3.2	175 (110)	200	35 ~ 50	30	30 ~ 35	MBE	a
InAsSb/InAsSP	3.5	130	–	33	250	–	MOCVD	b
InAsSb/InAsSP	3.6	–	100	23	–	–	LPE	c
InAsSb/InAlAsSb	3.9	165	30	–	78	16	MBE	d
Quantum Cascade Lasers:								
InGaAs/AlInAs	3.4	280	120 (15)	85	2.2k	–	MBE	e
InGaAs/AlInAs	5.0	300	200 (at 300 K)	150	8k (at 300 K)	–	MBE	f
InGaAs/AlInAs	8.0	300	1300 (at 100 K 325 (at 300 K)	107	8.5k (at 300 K)	–	MBE	g
Type II Superlattice Lasers:								
InAs/GaSb/GaInSb/GaSb	2.8 3.2 4.1	225 255 135	~100 ~100 ~50	– – –	600 (at 140 K) 760 (at 140 K) 2100 (at 120 K)	– – –	MBE	h
InAs/GaSb/GaInSb/GaSb	2.9	260	800 (100 K) 200 (200 K) 20 (250 K)	33	1.1k (at 200 K)	–	MBE	i
Center for Quantum Devices:								
InAsSb/InAsSbP	3.2	220 (140)	1000 (400) 3000 (3-stripe laser bar)	42	37	90 (up to 120 K)	MOCVD	j
InAsSb/InAsSbP/AlAsSb	3.4	–	1800 (400) 7000 (4-stripe laser bar)	54	250	40	MOCVD	k
InAsSb/InAsSbP	3.6	200	1000 (140)	110	40	70	MOCVD	l
InAsSb/InAsP SLS	4.06	140	546 (94)	35	100	–	MOCVD	
InAsSb/InAsSb SLS	4.26	150	183 (30)	40	100	–	MOCVD	
InAsSb/InAsSb SLS	4.47	–	460 (15)	–	285	–	MOCVD	
InAsSb/InAsSb SLS	4.76	–	230	–	445	–	MOCVD	
InP/AlInAs/GaInAs QCL	5.0	220	–	270	–	–	MBE	
InP/AlInAs/GaInAs QCL	7.3	300	300 (at 300 K) 1200 (at 80 K)	240	3290 (at 295 K)	–	MBE	
InP/AlInAs/GaInAs QCL	8.0	300	40 (at 300 K) 700 (at 80 K)	188	4.2k (at 300 K)	–	MBE	
InP/AlInAs/GaInAs QCL	9.5	200	17 (at 80 K)	188	–	–	MBE	

a) H.K. Choi et al, Electron. Lett. **32**, 1296 (1996); b) S. R. Kurtz et al, APL **68**, 1332 (1996); c) A. Popov et al, APL **68**, 2790 (1996); d) H. K. Choi et al, APL **67**, 2251 (1995); e) J. Faist et al, APL **72**, 680 (1998); f) J. Faist et al, APL **68**, 3680 (1996); g) C. Gmachl et al, AP, **72**, 3130 (1998); h) T. Hasenberg et al, J. Quantum Electron. **33**, 1403 (1997); i) W.W. Bewley et al. APL vol.71, 3607 (1997); j) A. Rybaltowski et al, APL **71**, 2430 (1997); k) D. Wu et al, APL March 1, 1999; l) B. Lane et al; APL **70**, 443 (1997).

where q is the superlattice wavenumber in the z (growth) direction. The constants k_i and μ_i are defined for i = 1, 2 as

$$k = \sqrt{\frac{3(E_c - E)[(E_{LH} - E)(E_{SO} - E) - 0.5\delta E_S^2]}{\hbar^2 p^2 [2(E_{SO} - \delta E_S - E) + E_{LH} - E]}} \quad (19)$$

$$\mu = \frac{3[0.5\delta E_S^2 - (E_{LH} - E)(E_{SO} - E)]}{p^2 [2(E_{SO} - \delta E_S - E) + E_{LH} - E]} \quad (20)$$

where E_c, E_{LH}, and E_{SO} are the energy of the conduction, light-hole, and spin-orbit split-off bands, respectively. δE_S is the strain induced shift of energies and P is the matrix element of the S and P type orbits:

$$P = <S|p_x|P> = <S|p_y|P> = <S|p_z|P> \quad (21)$$

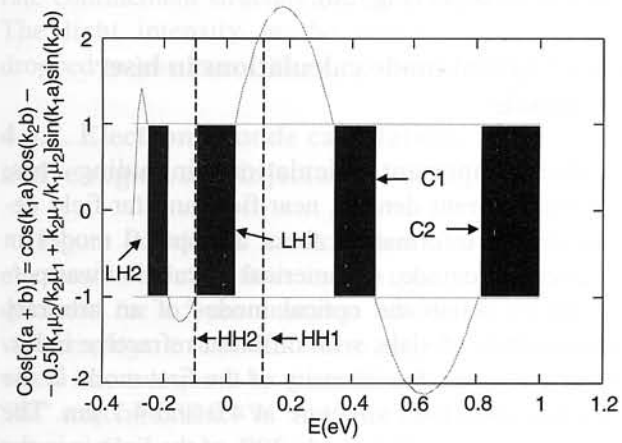

Fig. 26. Calculation of miniband energies of type II superlattice. C1 and C2 are the conduction minibands and LH1, LH2 and HH1 and HH2 are the light-hole and the heavy-hole minibands, respectively.

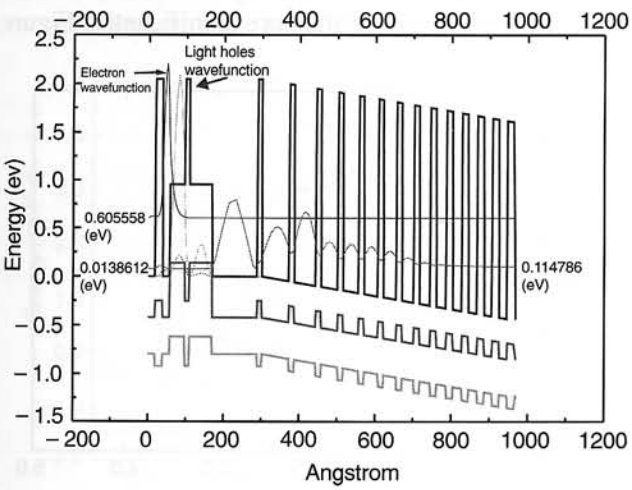

Fig. 27. Calculated wavefunctions of electrons and light holes of type II quantum cascade laser under electric field of E = 60 kV/cm.

In Eq. (18) the effect of strain which is important in this structure is also included explicitly. By numerically solving the spatial dependent Kane's Hamiltonian, Eq. (16), the wavefunction of the electrons and holes can be calculated for any given heterostructure at any electric field. Figure 26 shows the result of calculation of the minibands in an InAs/GaSb (48Å/48Å) superlattice. The calculation methods for wavefunctions are similar to bipolar counterpart. However, in this case, the effect of electric field on the band profile should be carefully considered.

Figure 27 shows the calculated wavefunctions of the electrons and holes in a type II quantum cascade laser with an electric field of ~ 60 kV/cm.

4.3. Type II InAs/GaSb/AlSb laser diodes for 3 ~ 4 μm wavelengths

The family of InAs–AlSb–GaSb have a very similar lattice constant. Despite small lattice mismatch, the layers of AlSb or InAs on GaSb substrates have a high density of misfit dislocation. For cladding layer, InAs/AlSb superlattices are typically used with the carefully calculated superlattice for an average lattice constant close to GaSb substrates. In this superlattice InAs layers are under tensile force while AlSb layers are under compressive force. The thickness of each layer should be calculated so that it counterbalances the effect of the next layer while the thickness is lower than the critical thickness of relaxation. Figure 28 shows the x-ray of one of the laser structures that are fabricated under these considerations. The sharp satellites with 70 arcsec FWHM shows excellent uni-

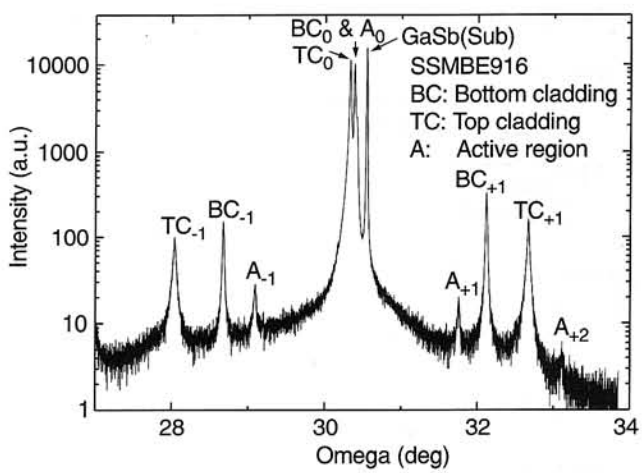

Fig. 28. High resolution diffraction x-ray of the laser structure shows excellent quality of the top and bottom cladding as well as the active layer. FWHM of the satellite are about 70 arcsec.

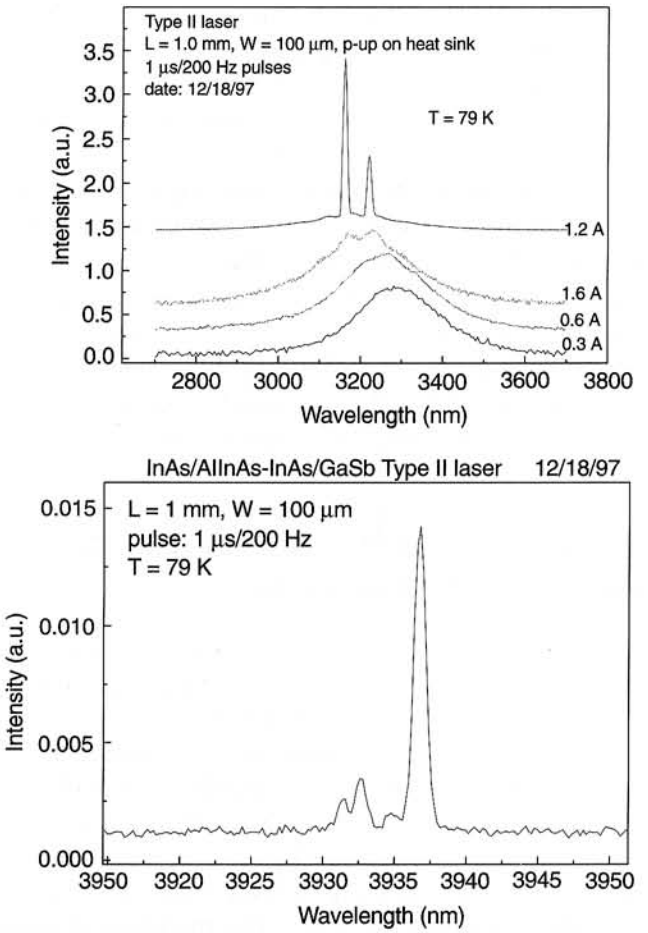

Fig. 29. Spectra of type II InAs/GaInSb/GaSb lasers at 79 K.

formity of the superlattices in the top and bottom cladding as well as the active layer [67].

These structures were grown in a Varian/EPI Modular GEN II solid source molecular beam epitaxy system on n–type GaSb substrates. Uncracked elemental As and Sb were used as source materials. The n–type cladding layer consists of a 12Å/10Å, InAs/AlSb superlattice. InAs layers were doped with silicon from n = 1×10^{18} cm^{-3} to n = 5×10^{17} cm^{-3} across the 1.1 μm cladding layer. A 70-period undoped InAs/GaInSb/GaSb (21Å/5Å/24Å) superlattice is used as the active layer. The p–type cladding layer is a 1.2 μm thick InAs–p/AlSb–p (16Å/13Å) superlattice which is doped with beryllium from p = 1×10^{17} cm^{-3} to p = 5×10^{18} cm^{-3}. The growths were terminated with a 200 Å InAs cap layer with a doping level of p = 10^{19} cm^{-3}. The preliminary results of the two recently grown samples show lasing at the calculated wavelengths of 3.2 μm and 3.9 μm wavelengths, Fig. 29. The characteristic temperature T_0 = 42 K of these lasers is significantly higher than the reported values of the type II lasers with superlattice active layer at 4 μm wavelength (Fig. 30).

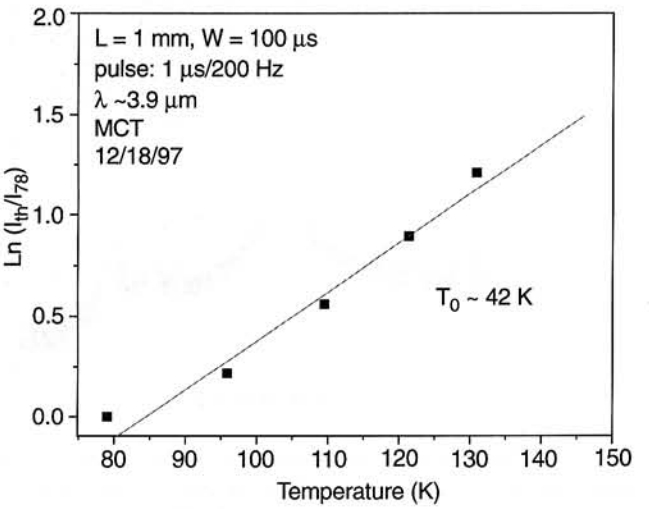

Fig. 30. Characteristic temperature T_0 is about 42 K.

4.3.1. Optical mode calculations in laser waveguide

Many important calculations including loss. threshold current density, near-field and far field depend on the information about the optical modes in the laser waveguide. A numerical calculation was performed to obtain the optical modes of an arbitrary configuration of slabs with different refractive index. Figure 31 shows the intensity of the first mode in the currently used laser structure at 4.0 and 4.7 μm. The calculation shows that nearly 30% of the light is in the cladding layer. This is important since the cladding layer is doped and free carrier absorption at this wavelength is considerably high. The calculation shows that a separate confinement structure can reduce the leakage out of the core significantly. Figure

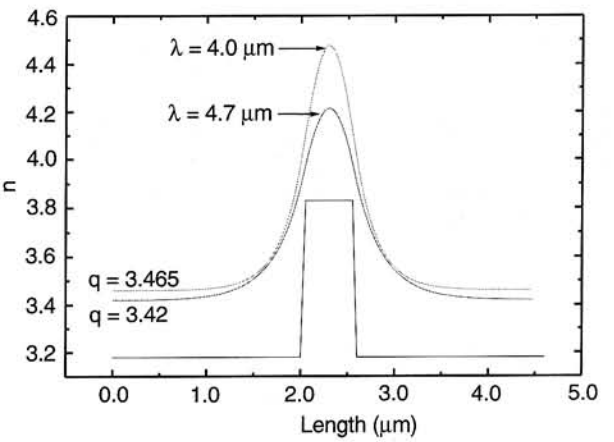

Fig. 31. The first optical mode of laser waveguide at 4.0 and 4.7 μm.

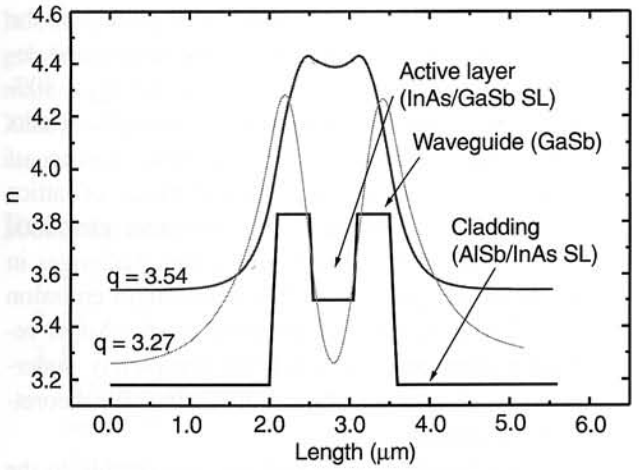

Fig. 32. The first and second optical modes in the separate confinement structure.

32 shows the first and second optical modes in a separate confinement structure designed for this purpose. The light intensity in the doped cladding layer dropped to less than 10% using this method.

4.3.2. Electronic mode calculations in the laser active region and injector

Figure 33 shows a calculation example for the electronic wavefunctions in the type II superlattices designed for 4.5-μm emission wavelength. This device employs a structure where active regions are divided into two parts by a small barrier, thus forming "W" structure. The "W" structure has several advantages such as:

1) Increase in the overlap of the electron and hole wavefunctions by nearly a factor of two;
2) Creation of a four-level laser rather than three--level and so higher population inversion can be achieved with the same carrier injection rate.

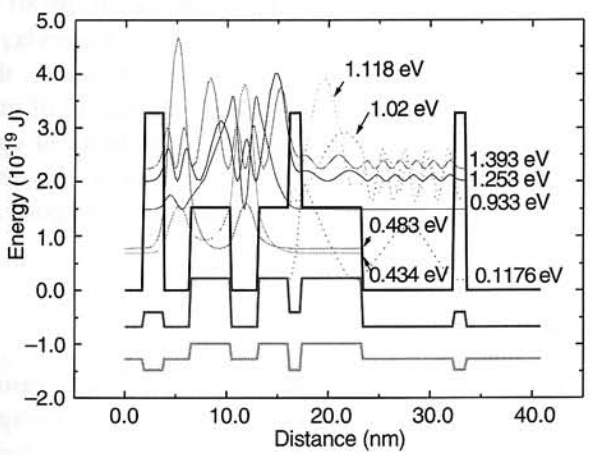

Fig. 33. Electrons and holes wavefunctions in a designed active layer for 4.5 μm wavelength.

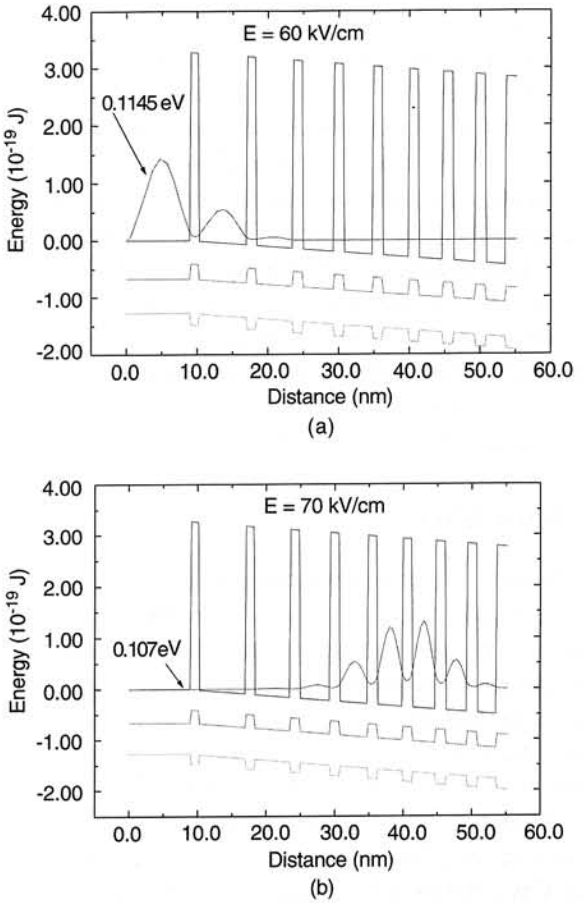

Fig. 34. (a) Electron wavefunction before and (b) after a turn-on electrical field.

The injector is particularly designed for: filtering of the electrons with incorrect energies at the designed electrical field; correct layer compositions for zero average mismatch to the substrate; and an energy difference equal to the laser wavelength from the beginning to the end of the injector. The laser was designed to work under about 70 kV/cm electrical field. Figures 34(a) and (b) show that in the correct injector design the electrons will start injection as the electrical field is increasing from 60 to 70 kV/cm. The calculation results illustrate that by properly adjusting electric field between 60 and 70 kV/cm, a resonance state (where electron distribution is almost uniform over the whole injector region) can be obtained, with a coherent injection of carriers from one stage to the next stage with high injection efficiency.

4.4. Future works

The current problems in the current technology for the type II superlattice lasers can be summarized as:

(i) The overlap of the electron and hole wavefunctions decreases rapidly at longer superlattice periods. Therefore, high performance lasers are

not expected for the longer wavelengths than 4 μm with the current device design.

(ii) The active or cladding layers may have very high loss due to the intraband transitions at the lasing wavelength. Detailed and accurate calculations are needed to avoid such problems.

(iii) The cladding and active layers are short-period strain compensated superlattices. Therefore, the quality of the growth is very sensitive to the composition of the interfaces.

(iv) The number of the grown layers in the current structures is about 1000 that is not likely to be practical in near future.

5. Summary

In such a rapidly developing subject as infrared lasers, any news becomes quickly obsolete. In this article, we attempted to review the theories and experimental results of infrared lasers for λ = 3 to 12 μm reported to date. Heat dissipation, and hardness of materials, maturity of growth and fabrication technology favors III–V-based lasers over the previously developed IV–VI and II–VI compounds-based lasers for the high power infrared lasers. For λ < 2.6 μm, room temperature CW operation now can be obtained from conventional type I GaInAsSb QW lasers with maximum output power over several tens mW. However for λ > 3 μm, high power laser operation (>300 mW) has been only limited to low operating temperature below 150 K due to the pronounced difficulties in growing high quality low band gap materials and fundamental physical limitation such as Auger recombination. For low temperature (below 150 K) laser operation with efficiency higher than 80% can be obtained from InAsSb-based broad-area DH and MQW lasers grown by MOCVD or MBE with output power high enough (> 300 mW) for most of applications considered. Maximum power up to 3 W has been obtained from a InAsSb/InPAsSb DH laser bar consisting of three 100-μm stripes with differential efficiency over 70% up to 150 K for λ = 3.6 μm. For longer wavelength (> 4 μm), lasers based on type II superlattice interband-transition show remarkable promise. Near room-temperature operation has been achieved for 3.5 μm < λ < 12 μm. However, yet these lasers showed a number of technological and intrinsic problems. The existing problems for the high-power infrared-semiconductor lasers can be summarized as follows:

(1) Experiment and theoretical models on InAsSb/InPAsSb-based lasers (far-fields, dependence of J_{th} on loss) showed that the lasers are significantly affected by the composition inhomogeneity of the active layer material in spite of otherwise good device characteristics (e.g. $J_{th} \sim 40$ A/cm^2, $\eta_d > 80\%$ at 77 K). This inhomogeneity essentially results from the thermodynamic unstable nature of In(P)AsSb alloys due to large difference of lattice constants and ionicities of constituent elements. This is one of the most fundamental challenges in the materials growth for this wavelength emission range. Also in spite of intensive study, Auger recombination process is not yet completely understood let alone the technical difficulties for theoretical calculation.

(2) The low band gap materials are susceptible to the even small amount of bulk- and interface-defects, degrading the function of pn junction, due to, e.g., impurity-assisted-tunneling. The much softer low band gap materials compared to higher band materials has relatively lower thermal conductivity, making the heat-dissipation the major issue in device design. We also discussed the "anomaly" in optical properties (far-field, cavity resonance frequencies) in InAsSb alloys, which may limit material combination for the heterostructure lasers.

(3) The novel class of mid-infrared lasers (Quantum Cascade Lasers) has shown promising results. However, still the power conversion efficiency is low, typically much less than 10%, prohibiting room temperature cw operation because of excessive heating. Physics related to carrier relaxation and tunneling as well as gain mechanisms in these lasers should be more precisely modeled in order to increase the efficiency of lasers.

(4) Type II bipolar and unipolar (cascade) lasers have shown impressive performance. T_o as high as 81 K was obtained up to T_{max} = 170 K from InAs/GaInSb/AlSb type II bipolar cascade lasers for λ = 3.85 μm with J_{th} = 290 A/cm^2 at 80 K [63]. High temperature performance, however, is yet to be seen. Like type I Sb-based lasers, the difficulty still remains the precise control of material growth, particularly reproducibility of cascaded QW regions. Presumably due to this reason, so far high power operation is not as good as type I Sb-based lasers.

Acknowledgments

The author would like to thank Dr. L.N. Durvasula and Dr. H.O. Everitt for their permanent encouragement and support, H. Yi for modelling and analysis, D. Wu and B. Lane for material growth of type I

InAsSb/InPAsSb lasers, H. Mohseni for material growth of type II InAs/GaInSb lasers, S. Slivken for material growth of intersubband QCL, J. Diaz and Y. Xiao for processing, and A. Rybaltowski for measurements.

References

1. K.J. Linden, *Proc. SPIE* **438**, 2 (1983).
2. M. Tacke, *Infrared Phys.* **36**, 447 (1995).
3. P. France, S. Carter, M. More, and J. Williams, "Optical loss mechanism in ZrF4 glasses and fibers", *Proc. 4th Int. Symp. Halide Glasses* **290** (1987).
4. S.H. Groves, K.W. Nill, and J. Strauss, *Appl. Phys. Lett.* **25**, 331 (1974).
5. J.N. Walpole, A.R. Calawa, T.C. Harman, and S.H. Groves, *Appl. Phys. Lett.* **28**, 552 (1976).
6. B. Spanger, U. Schiessl, A. Lambrecht, H. Bottner, and M. Tacke, *Appl. Phys. Lett.* **53**, 2582 (1988).
7. Z. Shi, M. Tacke, L. Lambrecht, and H. Bottner, *Appl. Phys. Lett.* **66**, 2537 (1995).
8. H. Choi, *CLEO'98, Semiconductor Laser Workshop*, San Fransicso, CA, May 8, 1998.
9. H.K. Choi, G.W. Turner, M.J. Manfra, and M.K. Connors, *Appl. Phys. Lett.* **68**, 2936 (1996a).
10. S.R. Kurtz, R.N. Biefeld, A.A. Allerman, A.J. Howard, M.H. Crawford, and M.W. Pelczynski, *Appl. Phys. Lett.* **68**, 1332 (1996).
11. B. Lane, D. Wu, A. Rybaltowski, H. Yi, J. Diaz, and M. Razeghi, *Appl. Phys. Lett.* **70**, 443 (1997).
12. D. Wu, E. Kass, J. Diaz, B. Lane, and A. Rybaltowski, H.J. Yi, and M. Razeghi, *IEEE Photon. Technol. Lett.* **9**, 173 (1997).
13. A. Rybaltowski, Y. Xiao, D. Wu, B. Lane, H. Yi, H. Feng, J. Diaz, and M. Razeghi, *Appl. Phys. Lett.* **71**, 2430 (1997).
14. C.H. Lin, R.Q. Young, D. Zhang, S.J. Murry, S.S. Pei, A.A. Allerman, and S.R. Kurtz, *Elec. Lett.* **33**, 598 (1997).
15. C.L. Felix, J.R. Meyer, I. Vurgaftman, C.H. Lin, S.J. Murry, D. Zhang, and S.S. Pei, *Phot. Tech. Lett.* **9**, 734 (1997).
16. J. Faist, F. Capasso, D.L. Sivco, C. Sirtori, A.L. Hutchinson, and A.Y. Cho, *Science* **264**, 553 (1994).
17. R.N. Hall, G.E. Fenner, J.D. Kingsley, T.J. Soltys, and R.O. Carlson, *Phys. Rev. Lett.* **9**, 366 (1962).
18. M.I. Natan, W.P. Dumke, G. Burns, F.H. Dill, Jr., and G. Lasher, *Appl. Phys. Lett.* **1**, 62 (1962).
19. T.M. Quist, R.H. Rediker, R.J. Keyes, W.E. Krag, B. Lax, A.L. McWhorter, and H.J. Zieger, *Appl. Phys. Lett.* **1**, 91 (1962).
20. K. Weiser and R.S. Levitt, *Appl. Phys. Lett.* **2**, 176 (1963).
21. M. Brown, P. Porteous, *Solid State Electron.* **10**, 76 (1967).
22. R.J. Phelan and R.H. Rediker, *Appl. Phys. Lett.* **6**, 70 (1965).
23. N. Basov, A. Dudenkova, A. Kraisilnikov, V. Nikitin, and K. Fedoseev, *Sov. Phys. Tech. Lett.* **8**, 847 (1966).
24. H.K. Choi, G.W. Turner, and M.J. Manfra, *Electron. Lett.* **32** ,1296 (1996).
25. A. A. Allerman, R.M. Biefeld, and S.R. Kurtz, *Appl. Phys. Lett.* **69**, 465 (1996).
26. C.A. Wang, K.F. Jensen, A.C. Jones, and H.K. Choi, *Appl. Phys. Lett.* **68**, 400 (1996).
27. D.M. Follstaedt, R. M. Biefeld, S.R. Kurtz, and K.C. Baucom, *J. Electron. Mater.* **24**, 819 (1995b).
28. R.M. Biefeld, K.C. Baucom, S.R. Kurtz and D.M. Follstaedt, *J. Cryst. Growth* **133**, 38 (1993).
29. B.L. Gelmont and G.G. Zegrya , *Sov. Phys. Semicond.* **25**, 1216 (1991); G.G. Zegrya, A.D. Andreev, N.A. Gun'ko, and E.V. Frolushkina, *Proc. SPIE* **2399**, 307 (1995).
30. H.J. Yi, *Ph. D. Thesis*, Northwestern University (1998).
31. M. Asada, A. Kameyama, and Y. Suematsu, *IEEE J. Quantum Electron.* **QE–20**, 745 (1984).
32. The quantum efficiency (the ratio of radiative recombination rate to total recombination rate) of this double heterostructure has been shown to be close to 100% below 150 K in our previous photoluminescence study [Lane et al., *Appl. Phys. Lett.* **70,** 1447 (1997)]. However, the differential efficiency (the ratio of optical output to electrical input power injected into the active region) of our lasers (0.1 W/A, or ~ 30%) is not as high as this value. The lower differential efficiency arises from the fact that some of the generated photons are absorbed or scattered inside the cavity, not contributing to the output power.
33. J. Diaz, H. Yi, A. Rybaltowski, B. Lane, G. Lukas, D. Wu, S. Kim, M. Erdtmann, E. Kass, and M. Razeghi, *Appl. Phys. Lett.* **70**, 40 (1997b).
34. Since the stripes are separated by 200 μm (which is much larger than the wavelength), coupling between them is negligible. These lasers function independently, with no phase coherence. The spectrum presented in Fig. 6 and 7 are results of incoherent superposition of multiple

number of lasers although it appears to originate from one laser. The narrow spectrum indicates high material uniformity across the bar.

35. M. Razeghi, H. Yi, and V. Litvinov, "High--power infrared semiconductor lasers (λ = 3 ~ 10 μm)", unpublished.
36. C.H. Henry, P.M. Petroff, R.A. Logan, and F.R. Merritt, *J. Appl. Phys.* **50**, 3721 (1979).
37. H. Casey and Panish, *Heterostructure Lasers*, Academic, New York, 1978.
38. D.M. Follstaedt, R.M. Biefeld, S.R. Kurtz, and K.C. Baucom, *J. Electron. Mater.* **24**, 819 (1995).
39. H. Yi, A. Rybaltowski, J. Diaz, D. Wu, B. Lane, Y. Xiao, and M. Razegh, *Appl. Phys. Lett.* **70**, 3236 (1997).
40. M . Razeghi, Nature **369**, 631 (1994); H. Yi, J. Diaz, L.J. Wang, I. Eliashevich, S. Kim, R. Williams, M. Erdtmann, X. He, E. Kolev, and M. Razeghi, *Appl. Phys. Lett.* **66**, 3251 (1995).
41. The refractive index for the ternaries InAsSb and quaternaries InPAsSb (shown in Table 2) are estimated from their constituent binary compounds by linear interpolation.
42. I. Skinner, R. Shail, and B. Weiss, *IEEE J. Quantum Electron.* **QE–25**, 6 (1989).
43. Strictly speaking, l_n arises from consideration of higher order of δn.
44. S. Adachi, *J. Appl. Phys.* **61**, 4689 (1987).
45. A. Haug, *Semicond. Sci. Technol.* **7**, 373 (1992).
46. A. Reisinger, P. Zory, Jr., and R. Waters, *IEEE J. Quantum Electron.* **23**, 993 (1987).
47. B. Lane, D. Wu, H. Yi, J. Diaz, A. Rybaltowski, S. Kim, M. Erdtmann, H. Jeon, and M. Razeghi, *Appl. Phys. Lett.* **70**, 1447 (1997).
48. R.F. Kazarinov, R.A. Suris, *Soviet Phys. Semiconductors* **5**, 707 (1971).
49. C. Sirtori, J. Faist, F. Capasso, D.L. Sivco, A.L. Hutchinson, and A.Y. Cho, *Appl. Phys. Lett.* **66**, 3242 (1995).
50. J. Faist, C. Gmachl, F. Capasso, C. Sirtori, D.L. Sivco, J.N. Baillargeon, and A.Y. Cho, *Appl. Phys. Lett.* **70**, 2670 (1997).
51. S. Slivken, C. Jelen, J. Diaz, M. Razeghi, *LEOS Newsletter* **11**(5), pp. 9–11, October 1997.
52. G. Strasser, P. Kruck, M. Helm, J.N. Heyman, L. Hvozdara, and E. Gornik, *Appl. Phys. Lett.* **71**, 2892 (1997).
53. J. Faist, F. Capasso, D.L. Sivco, A.L. Hutchinson, S.N.G. Chu, and A.Y. Cho, *Appl. Phys. Lett.* **72**, 680 (1998).
54. A. Tedicucci, F. Capasso, C. Gmachl, D. Sivco, A. Hutchinson, and A. Cho, "Multiple wavelength mid-infared lases operating on inter--miniband transitions", postdeadline papers, *CLEO'98*, San Fransicso, CA, May 3–8, 1998, paper CPD17, Optical Society of America, Washington DC (1998).
55. J. Faist, F. Capasso, C. Sirtori, D. Sivco, A. Hutchinson, and A. Cho, *Appl. Phys. Lett.* **67**, 3057 (1995).
56. G.A. Sai-Halasz, R. Tsu, and L. Esaki, *Appl. Phys. Lett.* **30**, 651 (1977).
57. G.A. Sai-Halasz, L.L. Chang, J.M. Welter, and L. Esaki, *Solid State Comm.* **27**, 935 (1978).
58. G.A. Sai-Halasz, and L. Esaki, *Phys. Rev.* B **18**, 2812 (1978).
59. L. Smith, C. Mailhiot, *J. Appl. Phys.* **62**, 2545 (1987).
60. R. Youngdale, J.R. Meyer, C.A. Hoffman, and F.J. Bartoli, *Appl. Phys. Lett.* **64**, 3160 (1994).
61. H. Xie, and W.I. Wang, *J. Appl. Phys.* **76**, 92 (1994).
62. J.L. Johnson, L.A. Samoska, A.C. Gossard, J. Merz, M.D. Jack, G.R. Chapman, B.A. Baumgratz, K. Kosai, and S.M. Johnson, *J. Appl. Phys.* **80**, 1116 (1996).
63. R.Q. Yang et al., *Appl. Phys. Lett.* **71**, 2409 (1997).
64. C.H. Grein, P.M. Young, and H. Ehrenreich, *J. Appl. Phys.* **76**, 1940 (1994).
65. M.E. Flatte, C.H. Grein, H. Ehrenreich, R.H. Miles, H. Cruz, *J. Appl. Phys.* **78**, 1995, pp. 4552–4559.
66. D. Gershoni, C. Henry, and G. Baraff, *IEEE J. Quantum Electron.* **QE–29**, 2433 (1993).
67. M. Razeghi and H. Mohseni, "λ = 3.9 μm InAs/GaInSb type II superlattice laser diodes", *CLEO '98*, Semiconductor Laser Workshop, San Francisco, CA, May 8 (1998).

